View Article Online
View Journal

Dalton Transactions

An international journal of inorganic chemistry

Accepted Manuscript

This article can be cited before page numbers have been issued, to do this please use: D. Basak, L. Smythe, R. Herchel, M. Murrie, I. Nemec and D. Ray, *Dalton Trans.*, 2021, DOI: 10.1039/D1DT02038B.

This is an Accepted Manuscript, which has been through the Royal Society of Chemistry peer review process and has been accepted for publication.

Accepted Manuscripts are published online shortly after acceptance, before technical editing, formatting and proof reading. Using this free service, authors can make their results available to the community, in citable form, before we publish the edited article. We will replace this Accepted Manuscript with the edited and formatted Advance Article as soon as it is available.

You can find more information about Accepted Manuscripts in the Information for Authors.

Please note that technical editing may introduce minor changes to the text and/or graphics, which may alter content. The journal's standard Terms & Conditions and the Ethical guidelines still apply. In no event shall the Royal Society of Chemistry be held responsible for any errors or omissions in this Accepted Manuscript or any consequences arising from the use of any information it contains.

ROYAL SOCIETY OF CHEMISTRY

rsc.li/dalton

View Article Online
DOI: 10.1039/D1DT02038B

From Tetranuclear to Pentanuclear [Co–Ln] (Ln = Gd, Tb, Dy, Ho) Complexes Across the Lanthanide Series: Effect of Varying Sequence of Ligand Addition

Dipmalya Basak,[a] Lucy Smythe,[b] Radovan Herchel,[c] Mark Murrie,[b] Ivan Nemec,[c,d] Debashis Ray*[a]

[a]*Department of Chemistry, Indian Institute of Technology, Kharagpur 721 302, India*

[b]*School of Chemistry, University of Glasgow, Glasgow, G12 8QQ, United Kingdom*

[c]*Department of Inorganic Chemistry, Faculty of Science, Palacky University, 17 Listopadu 12, Olomouc CZ-77146, Czech Republic*

[d]*Central European Institute of Technology, CEITEC BUT, Purkyňova 656/123, 61200 Brno, Czech Republic*

*E-mail: dray@chem.iitkgp.ac.in. Tel: (+91) 3222-283324. Fax: (+91) 3222-82252. Orcid: 0000-0002-4174-6445.

Abstract

Two new families of cobalt(II/III)–lanthanide(III) coordination aggregates have been reported: *Tetranuclear* $[Ln^{III}_2Co^{III}_2L_2(N–BuDEA)_2(O_2CCMe_3)_4(H_2O)_2]\cdot(MeOH)_n\cdot(H_2O)_m$ (Ln = Gd, **1**; Tb, **2**; Dy, **3**; n=2, m=10 for **1** and **2**; n=6, m=2 for **3**) and *Pentanuclear* $Ln^{III}_2Co^{II}Co^{III}_2L_2(N–BuDEA)_2(O_2CCMe_3)_6(MeOH)_2$ (Ln = Dy, **4**; Ho, **5**) formed from the reaction of two aggregation assisting ligands H_2L (*o*–vanillin oxime) and N–BuDEAH_2 (N–butyldiethanolamine). A change in preference from lower to higher nuclearity structure was observed on going across the lanthanide series brought about by the variation in size of the Ln^{III} ions. An interesting observation was made for the varying sequence of addition of the ligands in the reaction medium paving the way to access both structural types for Ln = Dy. HRMS (+ve) of solutions gave further insight into the formation of the aggregates via different pathways. The *tetranuclear* complexes adopt a modified butterfly structure with a more complex bridging network while trapping of an extra Co^{II} ion in the *pentanuclear* complexes destroy this arrangement putting the Co–Co–Co axis above the Ln–Ln axis. Direct current (dc) magnetic susceptibility measurements reveal weak antiferromagnetic coupling in **1**. Complexes **2** and **5** display no slow magnetic relaxation, whereas complexes **3** and **4** display out–of–phase signals at low temperature. All

View Article Online
DOI: 10.1039/D1DT02038B

compounds were analyzed with DFT and CASSCF calculations and information about the single-ion anisotropies and mutual 4*f*–4*f* / 4*f*–3*d* magnetic interactions were derived.

Introduction

The choice of ligand anions and solution phase reaction conditions are important parameters which can guide the synthesis of polynuclear aggregates although their formation is poorly understood and they are mostly synthesized serendipitously.[1] Recent efforts to understand the complex pathways for the aggregation processes has shed some light in this area.[2,3,4,5] During the past two decades, synthesis and characterization of multimetallic complexes based on 3*d* and 4*f* ions in single molecular entity have attracted great interest because of their potential single–molecule magnet (SMM) behaviour. The construction of polynuclear aggregates of desired shape with precise control over the position and coordination environment of the different types of metal ion is a challenge on its own. A possible strategy employed in the synthesis of 3*d*–4*f* molecules is the use of hard–soft donors for discriminatory coordination of 3*d* and 4*f* ions.[6] Though successful in certain aspects, this cannot help predict the structure of the final compound in polynuclear aggregate synthesis. Hence it is imperative to understand the mechanism of formation of coordination aggregates in order to advance the study of self–assembly.[7] In recent years mass spectrometry has become a useful tool for investigation of formation of cluster molecules in solution.[2,3,4,5,7,8]

The formation and nuclearity of coordination aggregates also depends on the electronic configuration and ionic radius of the metal ions, which consequently determines its coordination number.[9a] In the case of 4*f* metal ions the change in ionic radius across the series is more pronounced due to lanthanide contraction. The effect of this phenomenon on 3*d*–4*f* cluster formation has not been explored in detail for 4*f* metal ions.[9b,9c,9d] In a previous study we showed the effect of lanthanide ion size on the oxidation state of cobalt ions.[5b] The aim for the introduction of lanthanide ions in coordination clusters is to take advantage of their considerable single ion anisotropy and large spin[10] while the presence of 3*d* ions in close proximity to the 4*f* ions brings in stronger exchange interactions[11] compared to the weak 4*f*–4*f* dipolar interaction.[12] The $3d^7$ octahedral Co^{II} ion in high spin state is characterized by strong spin orbit coupling and its usefulness for slow magnetic relaxation is known.[13] On the other hand the presence of diamagnetic low spin Co^{III} in conjunction with paramagnetic Ln^{III} also tends to affect the magnetization reversal energy barrier.[14]

View Article Online
DOI: 10.1039/D1DT02038B

Compared to the study of assembly of coordination cluster molecules using one "key" ligand, studies of systems with mixed ligands possess greater difficulties due to competition between ligands.[15] In this respect use of ligands varying in denticity and coordination preferences is expected to simplify the issue. Phenol based oxime ligands are known to form homometallic as well as heterometallic polynuclear aggregates with or without the utilization of the bridging potency of the =N–O^{-} group.[16] Similarly polyalcohol amines tend to sequester multiple metal ions via their bridging alkoxido arms.[17] Substituted diethanolamines have been utilized for the synthesis of 3*d*–4*f* complexes with the familiar butterfly topology having the 4*f* ion in the body position.[18] Previously both these two types of ligands were used together for the synthesis of Mn_3Ln_4 clusters[19] but their formation was not investigated in detail nor could other structural types be accessed.

In this work we have utilized *o*-vanillin oxime (H_2L) in conjunction with N–Butyldiethanolamine (N–BuDEAH_2) (Chart 1) to explore their reactivity towards $Co_2(\mu\text{-}OH_2)(O_2CCMe_3)_4(HO_2CCMe_3)_4$ for the formation of $Co^{II/III}$–Ln^{III} aggregates. Interestingly a transition was observed from a *tetranuclear* $Ln^{III}{}_2Co^{III}{}_2$ structure to a *pentanuclear* $Ln^{III}{}_2Co^{II}Co^{III}{}_2$ structure on going across the lanthanide series (Ln = Gd, Tb, Dy, Ho). Interestingly, variation in the sequence of ligand addition gave access to both the structural types. HRMS analysis of solutions revealed the various pathways for formation of the aggregates made possible by the differential cleavage of the dinuclear structure of $Co_2(\mu\text{-}OH_2)(O_2CCMe_3)_4(HO_2CCMe_3)_4$ by the two ligands. The various binding modes of the pivalate ion observed in this work are represented in Chart S1.

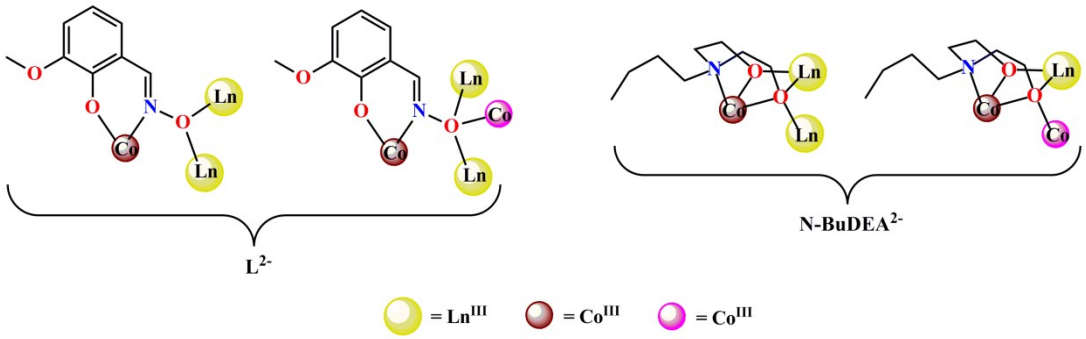

Chart 1. Metal ion coordination and bridging potential of L^{2-} and N–BuDEA^{2-} observed in this work.

View Article Online
DOI: 10.1039/D1DT02038B

Experimental Section

Reagents and starting materials. Chemicals used were obtained from the following sources: Cobalt carbonate, hydroxylamine hydrochloride and sodium acetate from SRL India; triethylamine from Merck, India; pivalic acid from Sigma Aldrich; $Gd(NO_3)_3{\cdot}6H_2O$, $Tb(NO_3)_3{\cdot}5H_2O$, $Dy(NO_3)_3{\cdot}5H_2O$, $Ho(NO_3)_3{\cdot}5H_2O$ and N–Butyldiethanolamine from Alfa Aesar; *o*-vanillin from Spetrochem, India. All other chemicals and solvents used in this work were reagent-grade materials and were used as received without further purification.

$Co_2(\mu\text{-}OH_2)(O_2CCMe_3)_4(HO_2CCMe_3)_4$ was prepared according to a literature procedure.[20] Cobalt carbonate (4.0 g, 34 mmol) was treated with an excess of pivalic acid (20.0 g, 196 mmol) in water (3 mL) at 100°C for 24 h, leading to dissolution of the carbonate salt. The solution was cooled to room temperature. MeCN (50 mL) was added and the mixture was briefly stirred. The solution was then filtered and cooled to 5 °C, yielding pink crystals within one day. The crystals were collected and the solution was then cooled to –4 °C for 2 days to give a second crop. The second crop was collected by filtration, washed with cold MeCN and dried in air. Yield = 65.8 %.

o-vanillin oxime was synthesized according to reported literature procedure.[16f]

Synthesis of Complexes

$[Ln^{III}_2Co^{III}_2L_2(N\text{–}BuDEA)_2(O_2CCMe_3)_4(H_2O)_2]{\cdot}(MeOH)_n{\cdot}(H_2O)_m$ (Ln = Gd, 1; Tb, 2; Dy, 3; n=2, m=10 for 1 and 2; n=6, m=2 for 3). All three tetranuclear complexes (**1–3**) were obtained by following a general synthetic protocol. A 5ml solution of $Co_2(\mu\text{-}OH_2)(O_2CCMe_3)_4(HO_2CCMe_3)_4$ (0.05 mmol) and $Ln(NO_3)_3{\cdot}xH_2O$ (0.1 mmol) in MeOH/DCM (2:1) was treated with N–Butyldiethanolamine ($N\text{–}BuDEAH_2$) (0.1 mmol) and stirred for 5 mins. H_2L (0.1 mmol) was added to the stirring solution followed by Et_3N (0.4 mmol) after another 5 mins. The resulting reddish brown solution was stirred for 3 h and filtered. The filtrate was left for slow evaporation of solvent and brown block shaped crystals suitable for single crystal X-ray analysis were formed over a period of 7 days. *When H_2L is added before $N\text{–}BuDEAH_2$ the same tetranuclear complexes were isolated for Ln = Gd, Tb but for Ln = Dy it gave rise to **4** the synthesis of which is discussed in the following section*. Details about the reactions and individual complexes are delineated below.

$[Gd^{III}_2Co^{III}_2]$ (1). $Co_2(\mu\text{-}OH_2)(O_2CCMe_3)_4(HO_2CCMe_3)_4$ (0.0474 g, 0.05 mmol), $Gd(NO_3)_3{\cdot}6H_2O$ (0.0451 g, 0.1 mmol), $N\text{–}BuDEAH_2$ (16.6 µL, 0.1 mmol), H_2L (0.0167 g, 0.1

View Article Online
DOI: 10.1039/D1DT02038B

mmol) and Et_3N (55.6 µL, 0.4 mmol). Yield: 0.035 g (40% based on Gd). Anal.Calcd (%) for $C_{54}H_{116}Co_2Gd_2N_4O_{32}$: C, 36.73; H, 6.62; N, 3.17. Found (%): C, 36.70; H, 6.67; N, 3.20. Selected IR peaks: (KBr, cm^{-1}, vs = very strong, br = broad, s = strong, m = medium, w = weak): 3152–3460 (br, $\tilde{\nu}_{OH}$), 1581 (s, $\tilde{\nu}_{C=N}$), 1568 (s, asym. $\tilde{\nu}_{COO}$), 1413 (s, sym. $\tilde{\nu}_{COO}$). UV-vis: λ_{max}, nm (ε, L mol^{-1} cm^{-1})] (MeOH) = 680 (66), 372 (2300), 298 (12100), 252 (44300), 218 (37300).

[$Tb^{III}_2Co^{III}_2$] (2). $Co_2(\mu\text{-}OH_2)(O_2CCMe_3)_4(HO_2CCMe_3)_4$ (0.0474 g, 0.05 mmol), $Tb(NO_3)_3{\cdot}5H_2O$ (0.0435 g, 0.1 mmol), N–$BuDEAH_2$ (16.6 µL, 0.1 mmol), H_2L (0.0167 g, 0.1 mmol) and Et_3N (55.6 µL, 0.4 mmol). Yield: 0.037 g (42% based on Tb). Anal.Calcd (%) for $C_{54}H_{116}Co_2Tb_2N_4O_{32}$: C, 36.66; H, 6.61; N, 3.17. Found (%): C, 36.69; H, 6.65; N, 3.19. Selected IR peaks: (KBr, cm^{-1}, vs = very strong, br = broad, s = strong, m = medium, w = weak): 3180–3490 (br, $\tilde{\nu}_{OH}$), 1581 (s, $\tilde{\nu}_{C=N}$), 1567 (s, asym. $\tilde{\nu}_{COO}$), 1412 (s, sym. $\tilde{\nu}_{COO}$). UV-vis: λ_{max}, nm (ε, L mol^{-1} cm^{-1})] (MeOH) = 682 (74), 374 (2000), 298 (11600), 252 (46200), 216 (24900).

[$Dy^{III}_2Co^{III}_2$] (3). $Co_2(\mu\text{-}OH_2)(O_2CCMe_3)_4(HO_2CCMe_3)_4$ (0.0474 g, 0.05 mmol), $Dy(NO_3)_3{\cdot}5H_2O$ (0.0438 g, 0.1 mmol), N–$BuDEAH_2$ (16.6 µL, 0.1 mmol), H_2L (0.0167 g, 0.1 mmol) and Et_3N (55.6 µL, 0.4 mmol). Yield: 0.039 g (45% based on Dy). Anal.Calcd (%) for $C_{58}H_{116}Co_2Dy_2N_4O_{28}$: C, 39.57; H, 6.64; N, 3.18. Found (%):C, 39.60; H, 6.67; N, 3.20. Selected IR peaks: (KBr, cm^{-1}, vs = very strong, br = broad, s = strong, m = medium, w = weak): 3214–3585 (br, $\tilde{\nu}_{OH}$), 1581 (s, $\tilde{\nu}_{C=N}$), 1570 (s, asym. $\tilde{\nu}_{COO}$), 1413 (s, sym. $\tilde{\nu}_{COO}$). UV-vis: λ_{max}, nm (ε, L mol^{-1} cm^{-1})] (MeOH) = 684 (110), 370 (2200), 298 (11600), 252 (41800), 216 (22200).

$Ln^{III}_2Co^{II}Co^{III}_2L_2(N\text{–}BuDEA)_2(O_2CCMe_3)_6(MeOH)_2$ (Ln = Dy, 4; Ho, 5). Both the pentanuclear complexes (**4**–**5**) were obtained by following a general synthetic procedure as in the case of **1**–**3** with only the order of addition of H_2L and N–$BuDEAH_2$ being reversed. A 5ml solution of $Co_2(\mu\text{-}OH_2)(O_2CCMe_3)_4(HO_2CCMe_3)_4$ (0.05 mmol) and $Ln(NO_3)_3{\cdot}xH_2O$ (0.1 mmol) in MeOH/DCM (2:1) was treated with H_2L (0.1 mmol) and stirred for 5 mins. N–Butyldiethanolamine (N–$BuDEAH_2$) (0.1 mmol) was added to the stirring solution followed by Et_3N (0.4 mmol) after another 5 mins. The resulting reddish brown solution was stirred for 3 h and filtered. The filtrate was left for slow evaporation of solvent and brown block shaped crystals suitable for single crystal X-ray analysis were formed over a period of 4 days. *When N–$BuDEAH_2$ is added before H_2L the same pentanuclear complex was isolated for Ln = Ho but in*

View Article Online
DOI: 10.1039/D1DT02038B

*much lower yield while for Ln = Dy it gave rise to **3** as described previously*. Details about the reactions and individual complexes are given below.

[$Dy^{III}_2Co^{II}Co^{III}_2$] (4). $Co_2(\mu\text{-}OH_2)(O_2CCMe_3)_4(HO_2CCMe_3)_4$ (0.0474 g, 0.05 mmol), $Dy(NO_3)_3{\cdot}5H_2O$ (0.0438 g, 0.1 mmol), H_2L (0.0167 g, 0.1 mmol), N–BuDEAH_2 (16.6 µL, 0.1 mmol) and Et_3N (55.6 µL, 0.4 mmol). Yield: 0.045 g (50% based on Dy). Anal.Calcd (%) for $C_{64}H_{110}Co_3Dy_2N_4O_{24}$: C, 42.20; H, 6.09; N, 3.08. Found (%): C, 42.17; H, 6.10; N, 3.10. Selected IR peaks: (KBr, cm^{-1}, vs = very strong, br = broad, s = strong, m = medium, w = weak): 3166–3482 (br, $\tilde{\nu}_{OH}$), 1579 (s, $\tilde{\nu}_{C=N}$), 1569 (s, asym. $\tilde{\nu}_{COO}$), 1412 (s, sym. $\tilde{\nu}_{COO}$). UV-vis: λ_{max}, nm (ε, L mol^{-1} cm^{-1})] (MeOH) = 688 (59), 540 (91), 442 (489), 374 (1500), 296 (9500), 252 (35600), 220 (19200).

[$Ho^{III}_2Co^{II}Co^{III}_2$] (5). $Co_2(\mu\text{-}OH_2)(O_2CCMe_3)_4(HO_2CCMe_3)_4$ (0.0474 g, 0.05 mmol), $Ho(NO_3)_3{\cdot}5H_2O$ (0.0451 g, 0.1 mmol), H_2L (0.0167 g, 0.1 mmol), N–BuDEAH_2 (16.6 µL, 0.1 mmol) and Et_3N (55.6 µL, 0.4 mmol). Yield: 0.046 g (51% based on Ho); 0.009 g (10% based on Ho when N–BuDEAH_2 is added before H_2L). Anal.Calcd (%) for $C_{64}H_{110}Co_3Ho_2N_4O_{24}$: C, 42.09; H, 6.07; N, 3.07. Found (%): C, 42.10; H, 6.10; N, 3.10. Selected IR peaks: (KBr, cm^{-1}, vs = very strong, br = broad, s = strong, m = medium, w = weak): 3324–3550 (br, $\tilde{\nu}_{OH}$), 1577 (s, $\tilde{\nu}_{C=N}$), 1547 (s, asym. $\tilde{\nu}_{COO}$), 1415 (s, sym. $\tilde{\nu}_{COO}$). UV-vis: λ_{max}, nm (ε, L mol^{-1} cm^{-1})] (MeOH) = 686 (115), 540 (158), 508 (125), 448 (624), 372 (1900), 298 (10200), 252 (36400), 220 (21800).

Physical Measurements. A PerkinElmer model 240C elemental analyzer was used to perform the elemental analyses (C, H and N). Solution electronic absorption spectra was recorded on a Shimadzu UV 3100 UV/Vis/NIR spectrophotometer while a PerkinElmer RX1 spectrometer were used to record the FTIR spectra. The electrospray ionization (ESI) high resolution mass spectra were collected on a Bruker Daltonics micrOTOF mass spectrometer.

SQUID measurements. All magnetic measurements were carried out on powdered crystalline samples restrained in eicosane using a Quantum Design MPMS 3 SQUID magnetometer. Data were corrected for the diamagnetic contribution of the sample holder and eicosane by measurements, and for the diamagnetism of each compound.

View Article Online
DOI: 10.1039/D1DT02038B

Theoretical calculations. The theoretical calculation at DFT level of theory were performed with ORCA 4.2 software.[21] The PBE0 hybrid functional[22] was used together with relativistic basis sets: SARC2-DKH-QZVP for Gd, Tb, Dy, Ho atoms, SARC2-DKH-QZV for Lu atoms, DKH-def2-TZVP for Co and DKH-def2-SVP for all other atoms.[23] The Douglas-Kroll-Hess Hamiltonian was used to treat relativistic effects[24] together with Gaussian finite nucleus model[25] and the increased radial integration accuracy for metal atoms was also set. The auxiliary basis set SARC/J[26] and the chain-of-spheres (RIJCOSX) approximation to exact exchange was also used.[27] Generally, the experimental X-ray structures of **1-3** were used for such calculations, in which hydrogen atoms positions were normalized in Mercury software.[28] In case of **4-5**, the truncated structures were used in which hydrogen atoms were optimized with PBE0 functional. The calculated spin densities were visualized with VESTA 3 program.[29]

The state average complete active space self–consistent field (SA-CASSCF) wave functions calculations were done with OpenMOLCAS 19.11[30] for **2-5** in such way that only one paramagnetic metal ion was preserved, and all others were replaced by diamagnetic ions. The active space was defined by five *d*-orbitals/seven *f*-orbitals and respective number of electrons for cobalt or lanthanide ions. The RASSCF method was used in the CASSCF calculations with the following numbers of multiplets: 7 septets, 140 quintets, 113 triplets, and 123 singlets for Tb^{III}, 21 sextets, 224 quartets, and 490 doublets for Dy^{III}, 35 quintets, 210 triplets, and 196 singlets for Ho^{III}, 10 quartets and 40 doublets for Co^{II}. In case of Tb^{III}, Ho^{III} and Co^{II}, all multiplets were included in the spin-orbit RASSI–SO procedure, while the number of states for Dy^{III} was limited as follows: 21 sextets, 128 quartets, and 130 doublets. ANO-RCC-VQZP was used for paramagnetic lanthanides, ANO-RCC-VTZP was applied for Co^{II} and also for all donor atoms (N/O) of the paramagnetic ions, and ANO-RCC-MB was used for the rest of atoms.[31]

Crystal Data Collection and Refinement. Single crystal X-ray diffraction data for **1**–**5** were collected on a Bruker SMART APEX-II CCD X-ray diffractometer furnished with a graphite-monochromated Mo Kα (λ = 0.71073 Å) radiation by the ω scan (width of 0.3° frame^{-1}) method at 100 K with a scan rate of 4 s per frame. SAINT and XPREP software[32] was used for Data processing and space group determination. Direct method of SHELXS-2014[33] was used to solve the structure and then refined with full-matrix least squares using the SHELXL-(2014/7)[34] program package included into WINGX system Version 2014.1.[35] Data were corrected for

View Article Online
DOI: 10.1039/D1DT02038B

Lorentz and polarization effects; an empirical absorption correction was applied using the SADABS.[36] The locations of the heaviest atoms (Ln and Co) were determined easily. The O, N and C atoms were subsequently determined from the difference Fourier maps. These atoms are refined anisotropically. In the absence of electron densities in the Fourier map the H atoms were incorporated at calculated positions and refined with fixed geometry and riding thermal parameters with respect to their carrier atoms. The crystals of **1**–**3** are susceptible to loss of crystallinity upon exposure to X–ray at room temperature making low temperature measurements a necessity and the best possible data has been presented. In **1** the C17 atom was highly disordered and refined isotropically. Residual electron densities were observed near (~ 0.84 Å) Tb1 in **1** which could not be modeled as any chemically sensible species. It is due to the presence of absorption artifacts caused by imperfections in absorption correction employed by the instrument. Such artifacts are sometimes observed when very heavy and strongly diffracting elements like lanthanides and actinides are present.[37] No unresolved twinning could be identified. Due to the presence of huge number of solvent molecules in close proximity to each other, some of H atoms could not be fixed unambiguously. Crystallographic diagrams were presented using DIAMOND software.[38] A summary of the crystal data and relevant refinement parameters is summarized in Table 1. Crystallographic data (including structure factors) have been deposited with the Cambridge Crystallographic Data Centre as supplementary publications CCDC–2090138, 2090137, 2090139, 2090141, 2090140. These data can also be obtained free of cost at www.ccdc.cam.ac.uk/conts/retrieving.html (or from the Cambridge Crystallographic Data Centre).

Table 1. Crystal data and structure refinement details for **1**–**5**

parameters	**1**	**2**	**3**	**4**	**5**
Formula	$C_{54}H_{116}Co_2Gd_2N_4O_{32}$	$C_{54}H_{116}Co_2Tb_2N_4O_{32}$	$C_{58}H_{116}Co_2Dy_2N_4O_{28}$	$C_{64}H_{110}Co_3Dy_2N_4O_{24}$	$C_{64}H_{110}Co_3Ho_2N_4O_{24}$
F.W. (g mol^{-1})	1765.87	1769.23	1760.41	1821.34	1826.20
crystal system	Triclinic	Triclinic	Triclinic	Monoclinic	Monoclinic
space group	$P\bar{1}$	$P\bar{1}$	$P\bar{1}$	$C\,2/c$	$C\,2/c$
Crystal color	Red	Red	Red	Red	Red
Crystal size / mm^3	0.20×0.17×0.15	0.22×0.20×0.17	0.21×0.18×0.14	0.22×0.19×0.16	0.25×0.20×0.19
a / Å	9.208(5)	9.070(7)	9.1793(4)	24.612(9)	24.397(5)
b / Å	13.808(10)	14.082(10)	13.7893(5)	17.542(6)	17.486(3)
c / Å	15.878(9)	15.886(13)	15.8210(6)	18.662(7)	18.601(3)
α	105.21(3)°	106.50(2)°	105.4240(10)°	90°	90°
β	99.60(2)°	99.44(3)°	99.8070(10)°	100.551(13)°	100.139(7)°

View Article Online
DOI: 10.1039/D1DT02038B

γ	102.95(4)°	101.78(2)°	103.0890(10)°	90°	90°
V / Å^3	1843(2)	1850(2)	1822.71(12)	7921(5)	7811(2)
Z	1	1	1	4	4
D_c / g cm^{-3}	1.591	1.587	1.604	1.527	1.553
μ / mm^{-1}	2.302	2.411	2.554	2.550	2.698
F(000)	906	1824	902	3708	3716
T / K	100(2)	100(2)	100(2)	100(2)	100(2)
Total reflns	21440	14501	21352	57120	43443
R(int)	0.0450	0.0449	0.0408	0.0752	0.1094
Unique reflns	6429	6376	6351	6920	6908
Observed reflns	5689	5466	5776	4752	4149
Parameters	439	439	442	513	498
R_1; wR_2 ($I > 2\sigma(I)$)	0.0376, 0.0922	0.0758, 0.1807	0.0324, 0.0832	0.0515, 0.1446	0.0558, 0.1406
GOF (F^2)	1.023	1.177	1.060	1.113	1.087
Largest diff peak and hole (e Å^{-3})	1.538, -0.910	3.123, -2.426	1.581, -1.034	1.313, -1.933	0.984, -1.490
CCDC No.	2090138	2090137	2090139	2090141	2090140

Results and Discussion

Synthetic Methodology. *o*-vanillin oxime (H_2L) was prepared according to a literature procedure by the reaction of *o*-vanillin and hydroxylamine hydrochloride in the presence of sodium acetate in aqueous medium.[16f] Coordination reactivity of H_2L together with N–Butyldiethanolamine (N–BuDEAH$_2$) with Cobalt and 4*f* metal ions were explored using $Co_2(\mu\text{-}OH_2)(O_2CCMe_3)_4(HO_2CCMe_3)_4$ and $Ln(NO_3)_3{\cdot}xH_2O$ (Ln = Gd, Tb, Dy, Ho) in the presence of Et_3N under varying order of ligand addition as summarized in Schemes 1 and 2. Reaction of $Co_2(\mu\text{-}OH_2)(O_2CCMe_3)_4(HO_2CCMe_3)_4$ and $Ln(NO_3)_3{\cdot}xH_2O$ (Ln = Gd, Tb, Dy) first with N-BuDEAH$_2$ followed by H_2L in the presence of Et_3N in a 0.5:1:1:1:4 molar ratio in MeOH/DCM under stirring condition resulted in deep brown solutions from which brown blocked shaped crystals of *tetranuclear* **1**–**3** were obtained in 40%, 42% and 45% yields, respectively (Eq. (1) and Scheme 1). Interestingly when $Co_2(\mu\text{-}OH_2)(O_2CCMe_3)_4(HO_2CCMe_3)_4$ and $Ln(NO_3)_3{\cdot}xH_2O$ (Ln = Dy, Ho) was initially reacted with H_2L followed by sequential addition of N–BuDEAH$_2$ and Et_3N (*order of addition of H_2L and N–BuDEAH$_2$ reversed*) in a 1:1:0.5:1:4 ratio in MeOH/DCM under stirring condition, it resulted in deep brown solutions from which brown blocked shaped crystals of *pentanuclear* **4** and **5** were obtained in 50% and 51% yields, respectively (Eq. (2) and Scheme 2). Complex **5** can also be synthesized by addition of N–BuDEAH$_2$ before H_2L but in much lower yields of 10%. When Ln = Gd, Tb, adding H_2L before N–BuDEAH$_2$ also resulted in tetranuclear **1** and **2**. Thus the preference of nuclearity of the

View Article Online
DOI: 10.1039/D1DT02038B

complexes changes from *four* to *five* on going *across the lanthanide series* with both the structural types being accessed when Ln = Dy through different sequence of addition of ligands in the reaction mixture.

$$2[Co^{II}{}_2(\mu-OH_2)(O_2CCMe_3)_4(HO_2CCMe_3)_4] + 4Ln(NO_3)_3 \cdot xH_2O + 4N-BuDEAH_2 + 4H_2L + 12Et_3N + nMeOH + O_2 \xrightarrow{MeOH-DCM} 2[Ln^{III}{}_2Co^{III}{}_2L_2(N-BuDEA)_2(O_2CCMe_3)_4(H_2O)_2] \cdot (MeOH)_n \cdot (H_2O)_m + 12\{(NHEt_3)(NO_3)\} + yH_2O + 8HO_2CCMe_3 \; [Ln = Gd, Tb, Dy \; (n = 2, m = 10 \; when \; Ln = Gd, Tb; n = 6, m = 2 \; when \; Ln = Dy; x = 6, y = 14 \; when \; Ln = Gd; x = 5, y = 10 \; when \; Ln = Tb; x = 5, y = 18 \; when \; Ln = Dy)] \cdots (1)$$

$$4Ln(NO_3)_3 \cdot 5H_2O + 3[Co^{II}{}_2(\mu-OH_2)(O_2CCMe_3)_4(HO_2CCMe_3)_4] + 4H_2L + 4N-BuDEAH_2 + 12Et_3N + 4MeOH + O_2 \xrightarrow{MeOH-DCM} 2[Ln^{III}{}_2Co^{III}{}_2Co^{II}L_2(N-BuDEA)_2(O_2CCMe_3)_6(CH_3OH)_2] + 12\{(NHEt_3)(NO_3)\} + 12HO_2CCMe_3 + 25H_2O \; [Ln = Dy, Ho] \cdots (2)$$

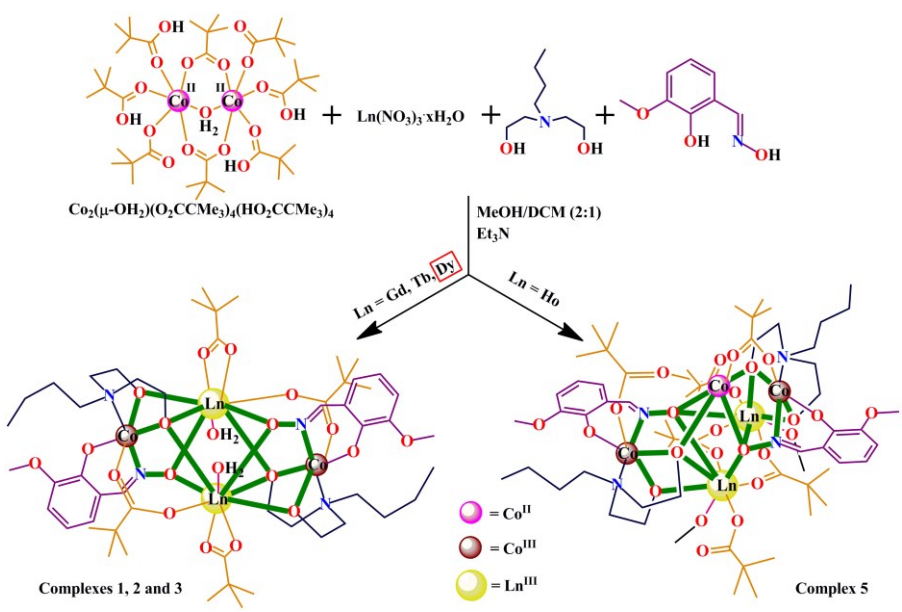

Scheme 1. Schematic representation for the formation of the complexes when N−BuDEAH$_2$ is added before H$_2$L.

View Article Online
DOI: 10.1039/D1DT02038B

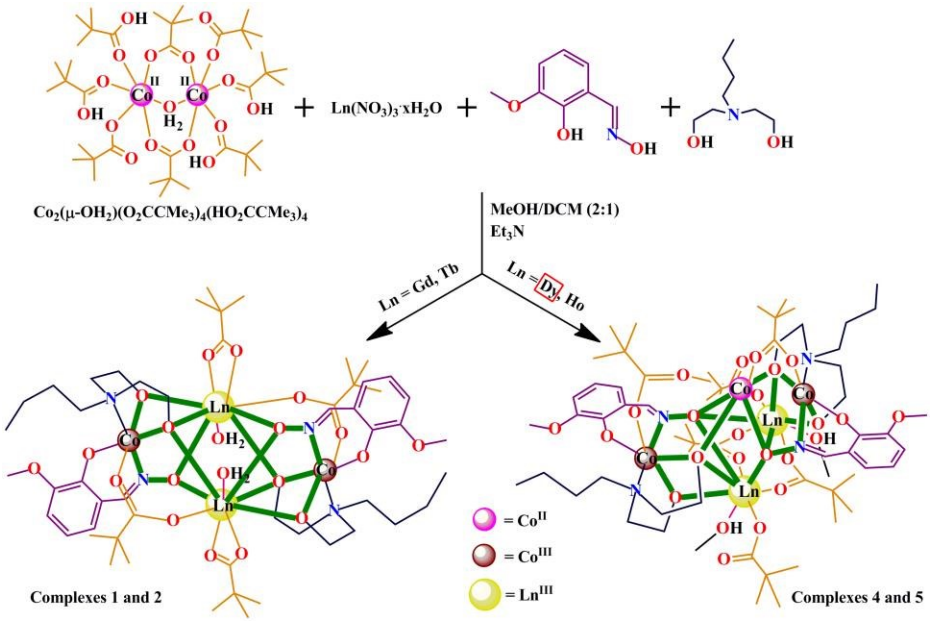

Scheme 2. Schematic representation for the formation of the complexes when H_2L is added before N–BuDEAH_2.

Single-crystal X-ray structure analysis revealed the formation of tetranuclear {$Ln^{III}{}_2Co^{III}{}_2$} (**1**–**3**) and pentanuclear {$Ln^{III}{}_2Co^{II}Co^{III}{}_2$} (**4**–**5**) neutral cores indicating that the varying course of addition of reactants and type of 4*f* ions do control the nature of aggregation process. Elemental analysis and initial physical characterizations (measured immediately after collection from crystallization mixture) were in good agreement with the molecular formula $C_{54}H_{116}Co_2Gd_2N_4O_{32}$, $C_{54}H_{116}Co_2Tb_2N_4O_{32}$ and $C_{54}H_{116}Co_2Dy_2N_4O_{32}$ for **1**–**3**, respectively and $C_{64}H_{110}Co_3Dy_2N_4O_{24}$ and $C_{64}H_{110}Co_3Dy_2N_4O_{24}$ for **4** and **5**. In **1**–**5**, **c**oordination of Co^{II} ions, derived from $Co_2(\mu\text{-}OH_2)(O_2CCMe_3)_4(HO_2CCMe_3)_4$, to L^{2-} and N–BuDEA^{2-} under aerobic condition lead to their oxidation to Co^{III}. The phenoxido O and N from =N–O$^-$ group in L^{2-} lend a bidentate coordination site for Co^{III} ions while the O end of =N–O$^-$, bridges two Ln^{III} ions in μ_2 fashion. The amine N of N–BuDEA^{2-} coordinates to the Co^{III} center *trans* to the N from =N–O$^-$. In **1**–**3**, one of the alkoxido arms of N–BuDEA^{2-}, bridges two Ln^{III} ions and a Co^{III} ion in μ_3 mode whereas the other connects one Ln^{III} and one Co^{III} ions in μ_2–bridging fashion. Unlike **1**–**3**, in **4** and **5** the μ_3 bridging alkoxido arm connects one Ln^{III}, one Co^{III} and a Co^{II} ion while the O end of =N–O$^-$ bridges two Ln^{III} and one Co^{II} in μ_3 fashion trapping an additional Co^{II} ion.

The tetranuclear cores of **1**–**3** can be described as having a butterfly like topology with folded wings with the Ln^{III} ions in the central body position and Co^{III} ions occupying the outer wing

View Article Online
DOI: 10.1039/D1DT02038B

positions. Unlike previously reported Co^{III}–4*f* butterfly structures the disposition of the metal ions and coordinating atoms within the core cannot be classified as partial dicubane or other known regular geometries (Chart 2, folding of wing tips shown by cyan circles) with the bridging network being more complex. Trapping of the additional Co^{II} ion in **4** and **5** destroys the butterfly like structure with two Co^{III} and one Co^{II} ions showing a nearly collinear arrangement having the Co–Co–Co axis placed above the Ln–Ln axis in a non–parallel manner (Figure 5).

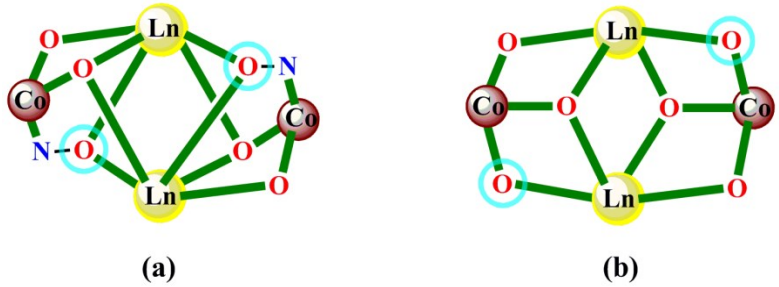

Chart 2. (a) Core of the butterfly like structure observed in present work and (b) partial dicubane core of previously reported butterfly structures. Folding of the wing tips in (a) compared to (b) are shown by cyan circles.

Description of crystal structures

$[Ln^{III}_2Co^{III}_2L_2(N–BuDEA)_2(O_2CCMe_3)_4(H_2O)_2]\cdot(MeOH)_n\cdot(H_2O)_m$ (Ln = Gd, 1; Tb, 2; Dy, 3; n=2, m=10 for 1 and 2; n=6, m=2 for 3). All the three complexes **1**–**3** crystallizes in triclinic $P\bar{1}$ space group with Z = 1. Selected metric parameters are listed in Table S1. The neutral tetranuclear complexes consist of a $\{Ln^{III}_2Co^{III}_2\}$ core having the general formula $Ln^{III}_2Co^{III}_2L_2(N–BuDEA)_2(O_2CCMe_3)_4(H_2O)_2$ formed with the help of two $L^{2–}$ and two N–$BuDEA^{2–}$ anions. The crystal lattices of **1** and **2** further accommodates ten water and two MeOH molecules while in **3** there are only two water and four MeOH molecules. The molecular structures of **1**–**3** are given in Figure 1. Since the complexes are isostructural, the structural description is given for the Gd derivative (**1**) as a representative case.

View Article Online
DOI: 10.1039/D1DT02038B

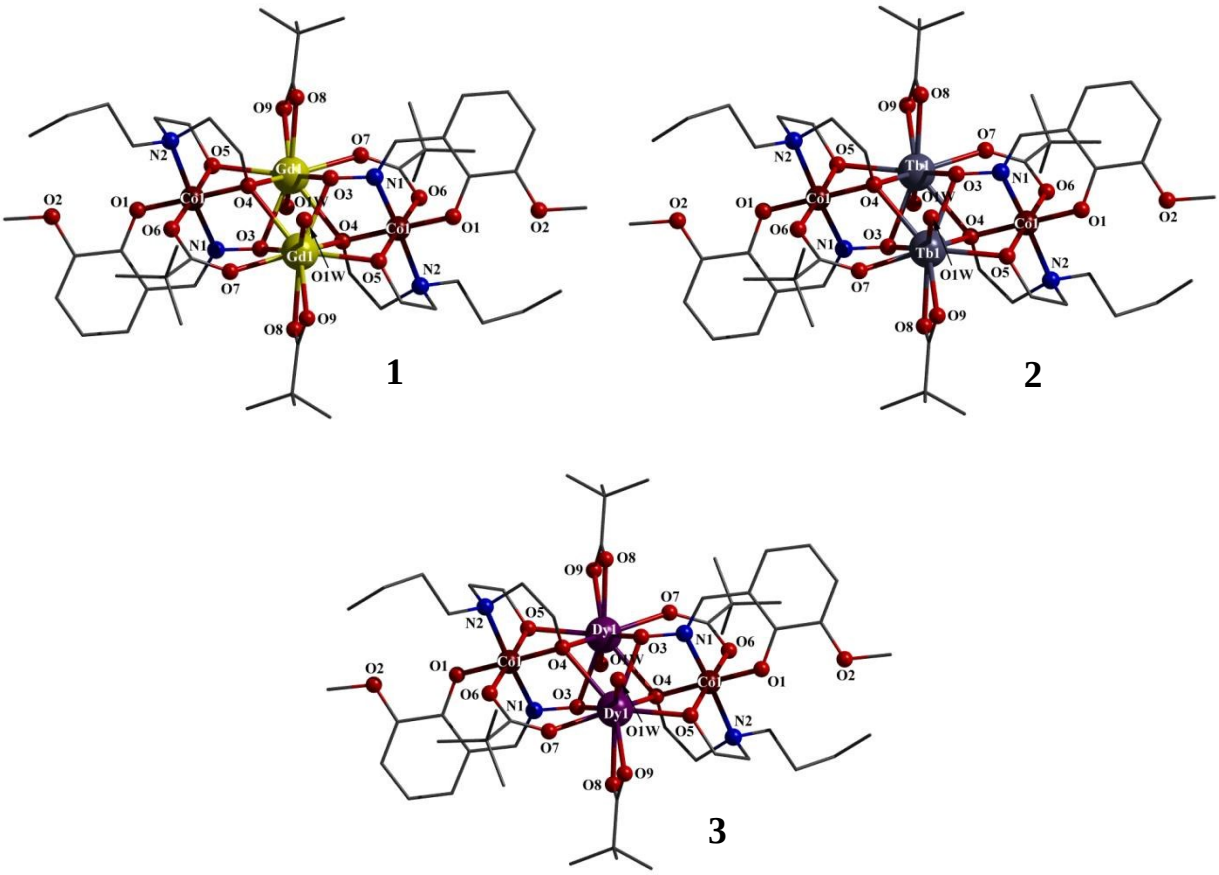

Figure 1. Molecular structures of **1**–**3**. Hydrogen atoms and solvent molecules are omitted for clarity. Colour code: Co^{III} brown, Gd^{III} yellow, Tb^{III} blue-grey, Dy^{III} violet, N blue, O red, S orange, C grey.

Each L^{2-} anion provides a bidentate ON coordination site for a 3*d* metal ion while a tridentate ONO coordination site is provided by the N–BuDEA^{2-} anion. Coordination of both L^{2-} and N–BuDEA^{2-} to a Co^{II} center derived from $Co_2(\mu\text{-}OH_2)(O_2CCMe_3)_4(HO_2CCMe_3)_4$ leads to its aerial oxidation to Co^{III}. Each L^{2-} anion coordinates to an octahedral Co^{III} ion in an *equatorial* manner while the N–BuDEA^{2-} anion shows a *facial* mode of coordination. The O end of hydroxyl amine group of each L^{2-}, in its deprotonated =N–O$^-$ form, bridges two Ln^{III} ions in a μ_2 fashion. One of the alkoxido arms of the N-BuDEA^{2-} further connects two Ln^{III} ions (in addition to Co^{III}) thus bridging the three metal centers in a μ_3 fashion. The other arm extends a μ_2–bridging mode towards an Ln^{III} ion connecting it to the Co^{III}. Additional capping coordination by two $Me_3CCO_2^-$ anions, obtained from $Co_2(\mu\text{-}OH_2)(O_2CCMe_3)_4(HO_2CCMe_3)_4$, between a Co^{III} and an Ln^{III} ion each in $\mu_{1,3}$ fashion lends further stability to the structure. Two more $Me_3CCO_2^-$ anions are consumed by the two Ln^{III} ions for η^2 chelation. Presence of a water molecule on the Ln^{III} ions fulfills the distorted Muffin geometry around them.

View Article Online
DOI: 10.1039/D1DT02038B

Figure 2 shows the various intermetallic separations within the $\{Gd_2O_2\}$ core of **1**. The O bridge from the =N–O$^-$ group of L^{2-} showed Gd1–O3 distances at 2.429(3) and 2.438(3) Å while connecting the two Gd^{III} centers asymmetrically (Figure S2). The μ_3 alkoxido arm of N–BuDEA^{2-} demonstrated different Gd1–O4 and Co1–O4 distances of 2.539(3), 2.558(4) and 1.904(3) Å respectively as did the μ_2 alkoxido arm for Gd1–O5 and Co1–O5 at 2.407(4) and 1.907(3) Å. Three different M–O–M angles were also recorded by the μ_3 alkoxido arm at 116.45(15)°, 97.05(13)° and 84.75(10)° corresponding to Co1–O4–Gd1 and Gd1–O4–Gd1. The bridge angle for the μ_2 alkoxido arm stands at 101.52(14)° (Co1–O5–Gd1) while that for the O end of =N–O$^-$ is 89.80(11)° (Gd1–O3–Gd1). The overall disposition of the four metal ion centers is more or less planar (Figure S3) with the bridging O atoms (O5) of μ_2 alkoxido arms lying in the plane through Co1 and Gd1 while those (O4) of the μ_3 alkoxido arm are displaced by 1.025 Å. The μ_3 O atom of =N–O$^-$ sits 1.487 Å away from this plane.

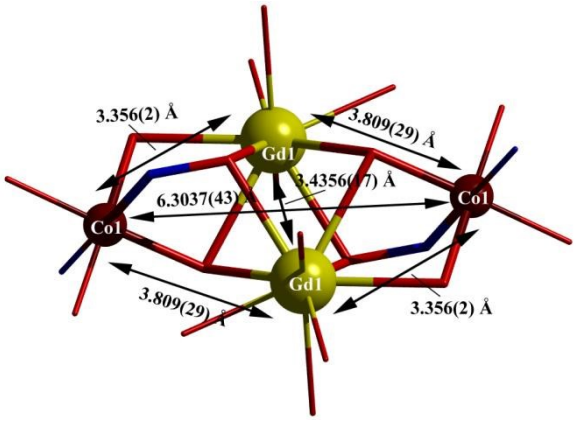

Figure 2. Intermetallic separations within the core of **1**. Color code: Co^{III} brown, Gd^{III} yellow, N blue, O red.

Continuous Shape Measures calculations show that the $\{O_9\}$ geometry around Gd1 is closer to Muffin (MFF; CShM = 1.311) as compared to Spherical Capped Square Antiprism (CSAPR; CShM = 1.570) (Figure S4a and Table S2). The triangular face comprising of O3, O4 and O5 is utilized for the formation of the butterfly like topology. A similar observation is made for the Ln^{III} ions in **2** and **3** (see Table S2 for CShM values). The Co^{III} centers on the other hand remain in a $\{N_2O_4\}$ distorted Octahedral environment (OC; CShM = 0.092 (**1**), 0.087 (**2**), 0.101 (**3**)) (Figure S4b and Table S3). The amine N from N–BuDEA^{2-} coordinates to the Co^{III} ion *trans* to the N from =N–O$^-$ of L^{2-} with a longer Co–N_{am} distance (Co1–N2, 1.990(4) Å) compared to the

View Article Online
DOI: 10.1039/D1DT02038B

Co–$N_{hyd\ am}$ distance (Co1–N1, 1.870(4) Å). Bond Valence Sum (BVS)[39] analysis for localized bonds around the metal ion centers validated a formal valence state of +III for Co1 and Dy1.

The numerous water and MeOH molecules present in the crystal lattice of **1** and **2** take part in extensive intermolecular hydrogen bonding interactions producing an infinite 3D network structure (Figure 3a). The O atoms from phenoxido (O1) and –OMe (O2) groups of L^{2-} trap a lattice water molecule (O6W) while a second water molecule (O5W) is trapped by the μ_2 alkoxido arm (O5) from N–BuDEA^{2-} together with O1 (Pink lines in Figures 3a and 3b). Both O6W and O5W further show hydrogen bonding interactions with a third water molecule (O4W) and together form a hydrogen bonded $(H_2O)_6$ cluster (Purple lines in Figures 3a and 3b) which connects the molecular units in one direction (Purple and pink lines in Figure 3a). Connection in the second direction is established through the hydrogen bonded interaction of a lattice water molecule (O2W) with the coordinated water molecule (O1W) and O8 of η^2–$Me_3CCO_2^-$ (Green lines in Figures 3a and 3c). O2W also shows interaction with O5W of the $(H_2O)_6$ cluster (Blue lines in Figure 3a). Another water molecule (O3W), hydrogen bonded to O4W, is further trapped by O1W and O9 of η^2–$Me_3CCO_2^-$ while a MeOH molecule (O10) shows interaction with this O3W as well as another MeOH (O10) thus connecting the molecular units in a third direction (Chrome yellow lines in Figure 3a and 3d). For the various parameters of the hydrogen bonding interactions refer to Table S4.

In contrast, the crystal lattice of **3** contains fewer water molecules and the hydrogen bonding interactions are far less extensive forming a 1D chain structure (Figure S5 and Table S4). Like in **1** and **2**, the lattice water molecule, O2W, shows interaction with O8 of η^2–$Me_3CCO_2^-$ and the coordinated water, O1W, connecting the molecular units in only one direction (Green lines in Figure S5). O1W and O9 of η^2–$Me_3CCO_2^-$ trap a MeOH molecule (O11) which in turn shows interaction with another MeOH (O10). A third MeOH molecule (O12) is trapped by O1 (phenoxido O) and O5 (μ_2 alkoxido arm) which shows further interaction with O2W.

View Article Online
DOI: 10.1039/D1DT02038B

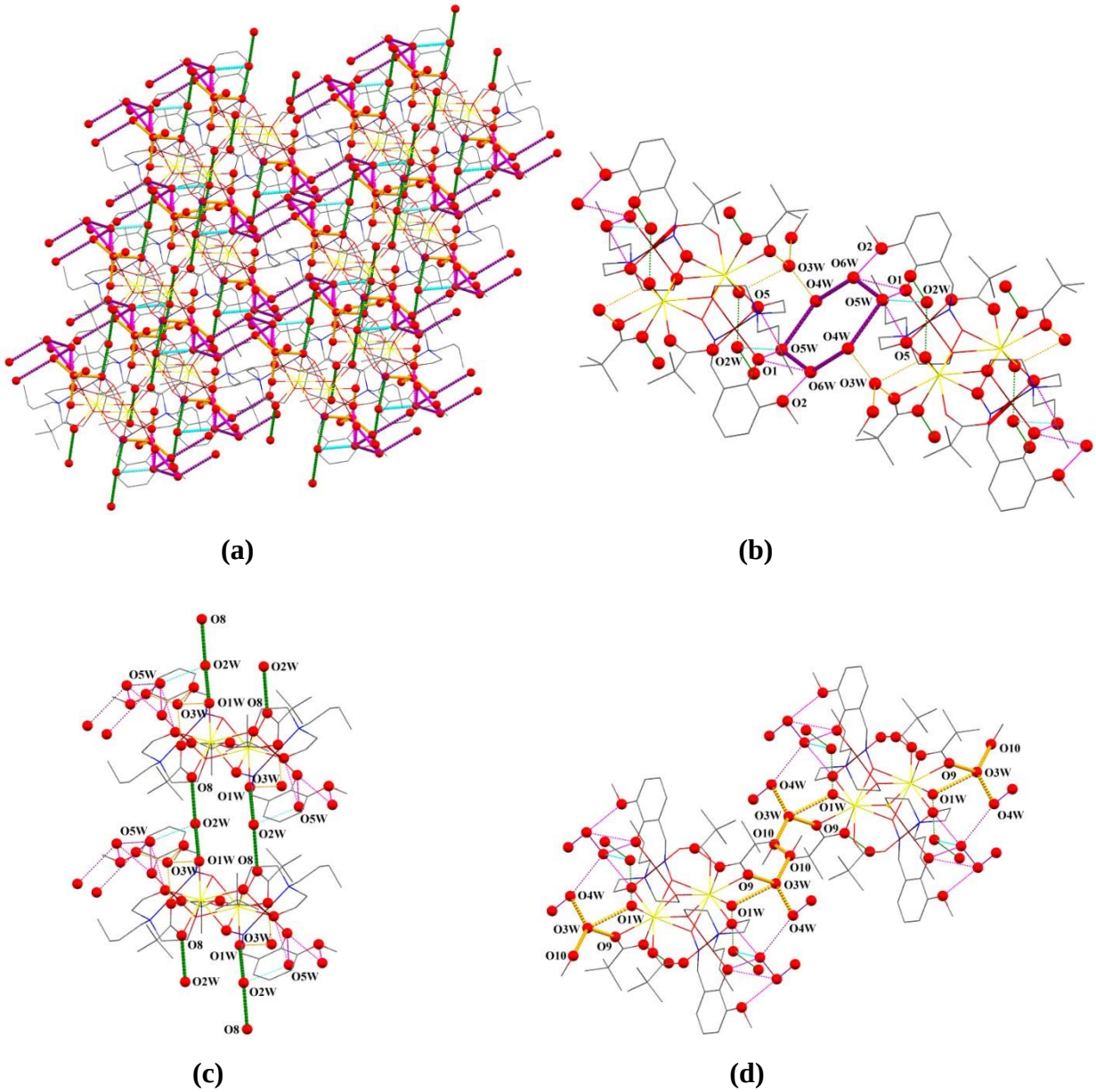

Figure 3. (a) Hydrogen bonded infinite 3D network structure formed with the help of lattice MeOH and H_2O molecules in **1**. (b) $(H_2O)_6$ cluster connecting molecular units in one direction. (c) Connection of molecular units in second direction via hydrogen bonding interactions between O8, O2W and O1W. (d) Hydrogen bonding interactions between O3W, O10 (lattice MeOH), O9, O1W and O4W connecting molecular units in third direction.

[$Ln^{III}_2Co^{II}Co^{III}_2L_2(N–BuDEA)_2(O_2CCMe_3)_6(MeOH)_2$] (Ln = Dy, 4; Ho, 5). Both the complexes **4** and **5** crystallizes in monoclinic *C* 2/c space group with Z = 4. Selected metric parameters are listed in Table S1. The neutral pentanuclear complexes consists of a $\{Ln^{III}_2Co^{III}_2Co^{II}\}$ core

View Article Online
DOI: 10.1039/D1DT02038B

having the general formula $Ln^{III}_2Co^{II}Co^{III}_2L_2(N–BuDEA)_2(O_2CCMe_3)_6(MeOH)_2$ formed with the help of two $L^{2–}$ and two $N–BuDEA^{2–}$ anions. The crystal lattice was found to be devoid of any solvent molecules. The molecular structures of **4** and **5** are presented in Figure 4. Both complexes are isostructural in nature and thus the structural description is presented for the Dy derivative (**4**) as a representative case.

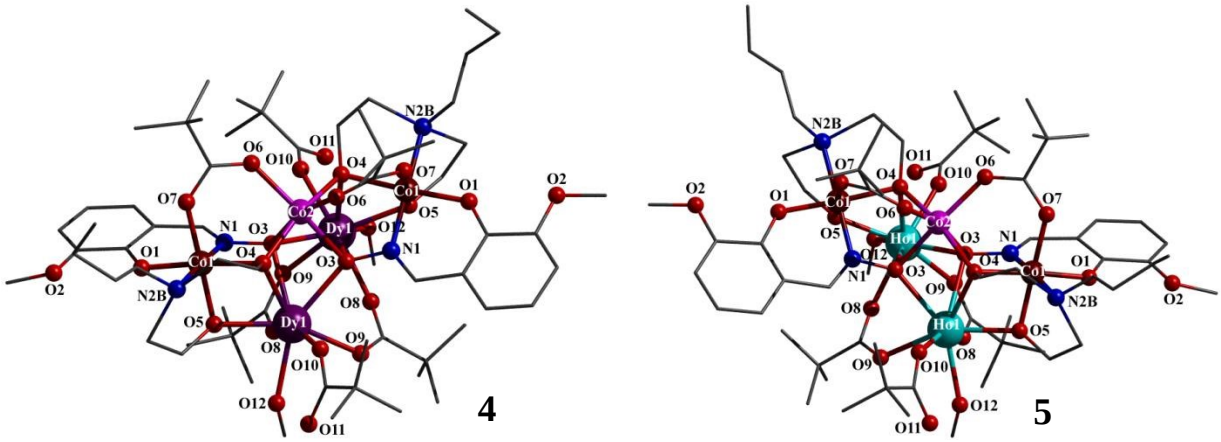

Figure 4. Molecular structures of **4** and **5** with atom numbering scheme and hydrogen atoms are omitted for clarity. Colour code: Co^{III} brown, Co^{II} pink, Dy^{III} violet, Ho^{III} turquoise, N blue, O red, C grey.

The coordination of $L^{2–}$ and $N–BuDEA^{2–}$ anions to the Co^{III} ion is similar to that described for **1**–**3**. In contrast, the μ_3 alkoxido arm of $N–BuDEA^{2–}$ connects a Ln^{III} and a Co^{II} ion (alongside Co^{III}) and not two Ln^{III} ions while the O end of the hydroxyl amine group of $L^{2–}$, in its deprotonated =N–O$^–$ form, bridges two Ln^{III} and the Co^{II} ion in a μ_3 fashion. Thus an additional Co^{II} ion, derived from $Co_2(\mu\text{-}OH_2)(O_2CCMe_3)_4(HO_2CCMe_3)_4$, is trapped in the structure of **4** and **5**. The bridging nature of the other alkoxido arm of $N–BuDEA^{2–}$ is similar (μ_2 connecting Co^{III} and Ln^{III}) to **1**–**3**. The Co^{II} ion is further connected to the Co^{III} ions by two $Me_3CCO_2^–$ anions, obtained from $Co_2(\mu\text{-}OH_2)(O_2CCMe_3)_4(HO_2CCMe_3)_4$, in $\mu_{1,3}$ fashion. Two more $Me_3CCO_2^–$ anions shows $\mu_{1,3}$–bridging connection between the two Ln^{III} ions instead of connecting Co^{III} with Ln^{III} as observed in **1**–**3** while two MeOH molecules coordinates to the Ln^{III} in place of water. The Ln^{III} ions further coordinate a $Me_3CCO_2^–$ anion each, in η^1 fashion in contrast with η^2 in **1**–**3** giving a $\{O_8\}$ distorted Square Antiprism geometry around them instead of $\{O_9\}$.

The various intermetallic separations within the $\{Dy_2Co_3\}$ core of **4** are presented in Figure 5. The O end of =N–O$^–$ showed greater variation in the two Dy1–O3 distances at 2.422(5) and 2.583(5) Å compared to **1**–**3** while the Co2–O3 distance is much shorter at 2.102(5) Å (Figure

View Article Online
DOI: 10.1039/D1DT02038B

S6). The μ_3 alkoxido arm of N–BuDEA^{2-} also showed three different bond distances for Dy1–O4, Co2–O4 and Co1–O4 at 2.537(5), 2.049(5) and 2.005(7) Å while at the same time giving different M–O–M angles of 108.5(2)° (Co1–O4–Co2), 94.26(18)° (Co2–O4–Dy1) and 92.5(2)° (Co1–O4–Dy1). The μ_2 alkoxido arm recorded two Dy1–O5 and Co1–O5 distances at 2.306(6) and 1.880(6) Å and a Co1–O5–Dy1 angle of 103.6(3)°. The three bridge angles for the O end of =N–O$^-$ stands at 99.2(2)°, 96.3(2)° and 91.69(19)° for Dy1–O3–Dy1, Co2–O3–Dy1 and Co2–O3–Dy1. In contrast to **1**–**3** the overall disposition of the metal ion centers in **4**–**5** are not planar, rather the cobalt centers (Co1 and Co2) are more or less collinear with the Co–Co–Co axis lying above the Dy–Dy axis. Thus the two planes containing one Co1 and two Dy1, each, make an angle of 82.18° (Figure S7a) while those through Co1, Co2 and Dy1, Co2 are inclined at 50.25° (Figure S7b).

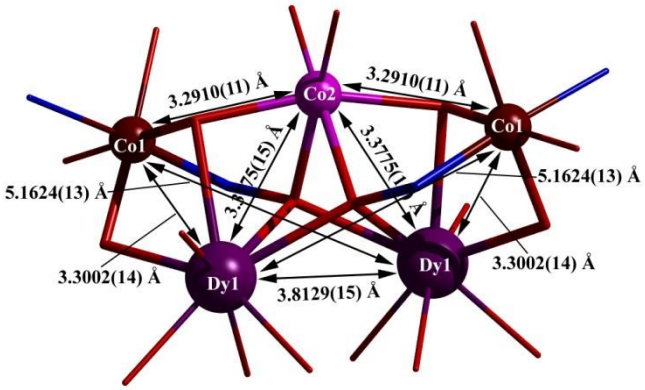

Figure 5. Intermetallic separations within the core of **4**. Color code: Co^{III} brown, Co^{II} pink, Dy^{III} violet, N blue, O red, C grey.

Continuous Shape Measures calculations show that the {O_8} geometry around Dy1 is closest to Square Antiprism (SAPR; CShM = 1.491) (Figure S8a and Table S2) with the two triangular faces comprising of O3, O4, O5 and O3, O3, O4 being utilized for the formation of {Dy_2Co_3} core. The Co^{III} and Co^{II} centers on the other hand remain in {N_2O_4} and {O_6} distorted Octahedral environments (OC; CShM = 0.436, Co1 and 1.103, Co2) (Figures S8b and S8c and Table S3). Similar observations are made for **5** (see Tables S2 and S3 for values). As is evident from the CShM values, the Co^{II} center accommodates a higher distortion of the Octahedral geometry compared to Co^{III}. Like **1**–**3**, the amine N from N–BuDEA^{2-} coordinates to the Co^{III} ion *trans* to the N from =N–O$^-$ of L^{2-} with a longer Co–N_{am} distance (Co1–N2B, 1.004(17) Å) compared to the Co–$N_{hyd\ am}$ distance (Co1–N1, 1.893(6) Å). Bond Valence Sum (BVS)[39]

View Article Online
DOI: 10.1039/D1DT02038B

analysis for localized bonds around the metal ion centers validated a formal valence state of +III for Co1 and Dy1, and +II for Co2.

The crystal lattices of **4** and **5** are devoid of any solvent molecules and hence no hydrogen bonded supramolecular structures are observed. Only intra molecular interaction is present between O12 of the coordinated MeOH and O11 of η^1 $Me_3CCO_2^-$ anions (Table S4).

Rationale for the observed difference in structural types

In order to understand the effect of different sequence of ligand addition on the structure of the final compound, we have analyzed the HRMS (+ve) of the reaction mixtures (in MeOH) for addition of N–BuDEAH_2 before H_2L and vice versa (Figures S9 to S16) in search of logical intermediates. Since both the structural types can be accessed for Ln^{III} = Dy^{III}, analysis of the mass spectra of **3** and **4** gives information about the two aggregation processes.

The mass spectra for **3** revealed two peaks at *m*/*z* = **273.0982** and **385.1170** which can be assigned to the mononuclear Co^{II} and Co^{III} species $\mathbf{\{Co^{II}(N–BuDEAH)(H_2O)_3\}^+}$ ($C_8H_{24}CoNO_5$; calcd. 273.0986) and $\mathbf{\{Co^{III}(HL)(N–BuDEA)\}^+}$ ($C_{16}H_{26}CoN_2O_5$; calcd. 385.1174) respectively (Figure S13). Such mononuclear species (Scheme 3, species **a** and **b**) are formed by the initial coordination of N–BuDEAH^- to a Co^{II} ion, after dissociation of $Co_2(\mu\text{-}OH_2)(O_2CCMe_3)_4(HO_2CCMe_3)_4$, followed by HL^- leading to its oxidation when N–BuDEAH_2 is added before H_2L. The mass spectra further exhibits a peak at *m*/*z* = **485.1269** which can be assigned to the species $\mathbf{\{[Dy^{III}_2(O_2CCMe_3)_6(H_2O)_2]+2H\}^{2+}}$ ($C_{30}H_{60}Dy_2O_{14}$; calcd. 485.1266). This points to the *in-situ* formation of dinuclear Dysprosium pivalate in reaction medium (Scheme 3). Previously we had reported the formation and presence of mononuclear $Ln(\eta^1\text{-}O_2CCMe_3)_2(\eta^2\text{-}O_2CCMe_3)_2(CH_3OH)_2^-$ counter anions within the crystal lattice.[5] Trapping of the Dysprosium pivalate by two mononuclear species **b** by extending a bridging coordination mode from the O atoms of alkoxido arms and =N–O^- group, lead to the formation of the tetranuclear $Dy^{III}_2Co^{III}_2$ complex (Scheme 3, intermediate **c**). The $\mu_{1,3}$ $Me_3CCO_2^-$ bridges between two Dy^{III} ions in Dysprosium pivalate are removed during such a process. The presence of complex **3** in solution is confirmed from the peak at *m*/*z* = **1571.2845** corresponding to $\mathbf{\{[Dy^{III}_2Co^{III}_2L_2(N–BuDEA)_2(O_2CCMe_3)_4(H_2O)_2]+K\}^+}$ ($C_{52}H_{88}Co_2Dy_2KN_4O_{20}$; calcd. 1571.2853).

View Article Online
DOI: 10.1039/D1DT02038B

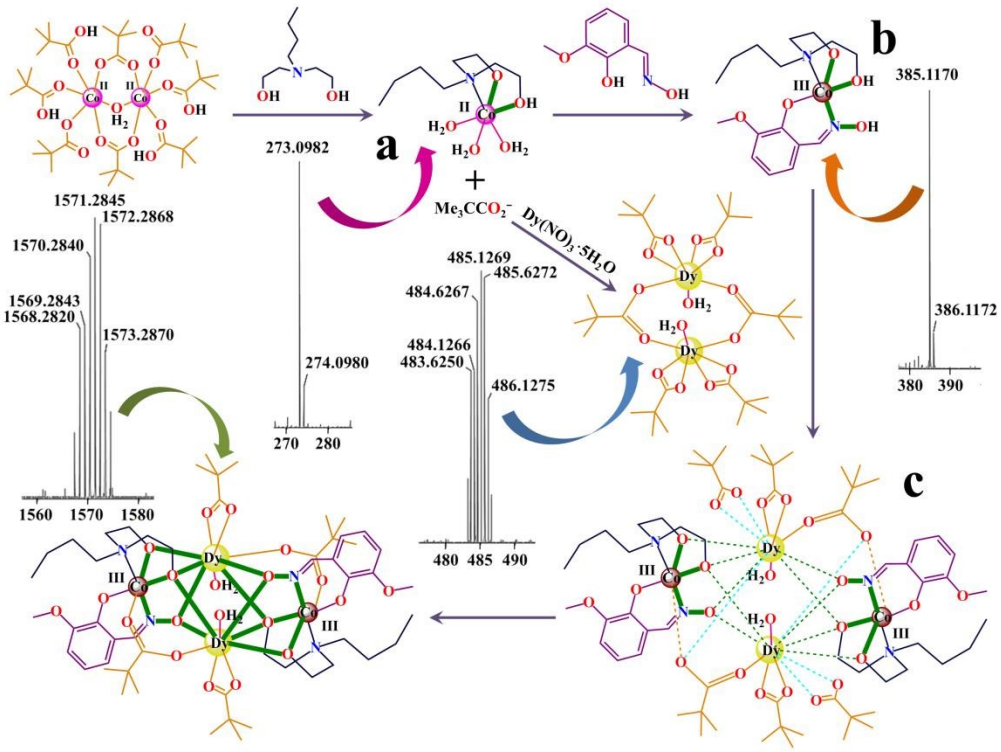

Scheme 3. Proposed pathway for the formation of **3** in MeOH medium with N–BuDEAH$_2$ being added before H$_2$L.

In the case of **4**, the two peaks at *m*/*z* = **512.0745** and **608.1558** can be assigned to the dinuclear Co^{II}_2 and $Co^{II}Co^{III}$ species **{Co^{II}_2(HL)(O_2CCMe_3)(MeOH)$_4$}$^+$** ($C_{17}H_{32}Co_2NO_9$; calcd. 512.0741) and **{$Co^{II}Co^{III}$L(N–BuDEAH)(O_2CCMe_3)(MeOH)$_2$}$^+$** ($C_{23}H_{42}Co_2N_2O_9$; calcd. 608.1554) respectively (Figure S14). Such dinuclear species (Scheme 4; species **a** and **b**) arise from the initial coordination of L^{2-} to $Co_2(\mu\text{-}OH_2)(O_2CCMe_3)_4(HO_2CCMe_3)_4$ followed by N–BuDEAH$^-$, leading to the oxidation of one cobalt center, when H$_2$L is added before N–BuDEAH$_2$. Thus unlike N–BuDEAH$_2$ (in **3**), initial coordination of H$_2$L to $Co_2(\mu\text{-}OH_2)(O_2CCMe_3)_4(HO_2CCMe_3)_4$ results in preservation of its dinuclear structure. A peak at *m*/*z* = **1029.2724** can be assigned to the trinuclear $Co^{II}Co^{III}_2$ species **{$Co^{II}Co^{III}_2$L$_2$(N–BuDEAH)$_2$(O_2CCMe_3)$_2$}$^{\bullet+}$** ($C_{42}H_{68}Co_3N_4O_{14}$; calcd. 1029.2728) (Scheme 4; species **c**) formed from two species **b** through the loss of a Co^{II} ion. Like in **3**, the peak at *m*/*z* = **485.1269** corresponding to **{[Dy^{III}_2(O_2CCMe_3)$_6$(H_2O)$_2$]+2H}$^{2+}$** points to the formation of dinuclear Dysprosium pivalate which is trapped by the species **c**, through extension of bridging coordination mode from the O atoms of alkoxido arms and =N–O$^-$ group, leading to the formation of the pentanuclear $Dy^{III}_2Co^{II}Co^{III}_2$ complex (Scheme 4; intermediate **d**). Unlike in **3**, the $\mu_{1,3}$ $Me_3CCO_2^-$ bridges between the two Dy^{III} ions in

View Article Online
DOI: 10.1039/D1DT02038B

Dysprosium pivalate remain intact during such a process. The peak at *m*/*z* = **933.6923** corresponding to **{[Dy^{III}$_2$Co^{II}Co^{III}$_2$L$_2$(N–BuDEA)$_2$(O$_2$CCMe$_3$)$_6$(MeOH)$_2$]+2Na}$^{2+}$** ($C_{64}H_{110}Co_3Dy_2N_4Na_2O_{24}$; calcd. 933.6925) confirms the presence of complex **4** in solution.

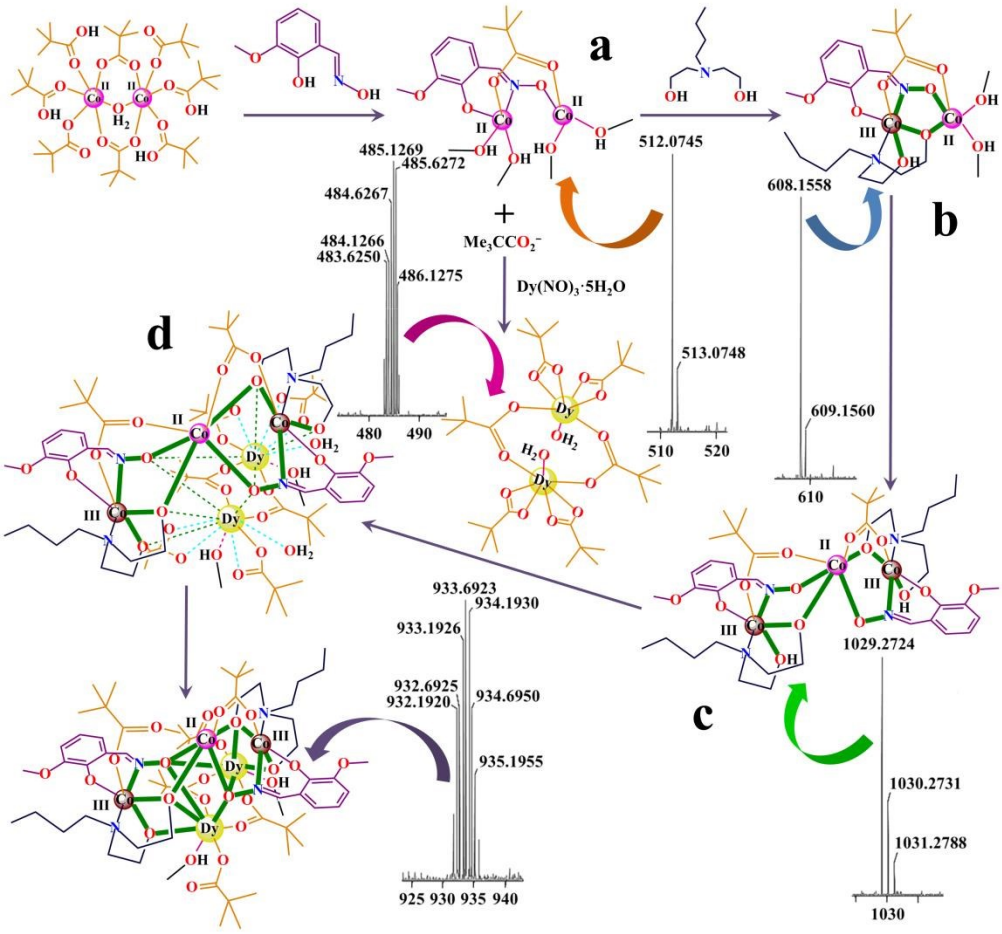

Scheme 4. Proposed pathway for the formation of **4** in MeOH medium with H_2L being added before N–BuDEAH$_2$.

For **1** and **2**, when N–BuDEAH$_2$ is added first, the formation of both follows a pathway similar to **3** through intermediate **e** (Scheme S1, Path I). When H_2L is added first, the formed dinuclear species **d** (similar to that described for **4**) looses a Co^{II} ion to give rise to mononuclear species **b** which results in **1** and **2** through intermediate **e** as shown for **3** (Scheme S1). In case of **5**, for addition of H_2L before N–BuDEAH$_2$ (Scheme S2; Path I), the aggregation pathway leading to its formation is similar to **4**. But when N–BuDEAH$_2$ is added before H_2L (Scheme S2, Path II), two of the formed mononuclear species **b** (similar to that described for **3**) traps a Co^{II} ion leading to

View Article Online
DOI: 10.1039/D1DT02038B

the trinuclear species **e** which follows the usual pathway as shown for **4**. A detailed description for **1**, **2** and **5** is presented in ESI.

The impetus towards the transition from *tetranuclear* to *pentanuclear* structure across the lanthanide series is provided by the decreasing size of Ln^{III} ions and their consequent preference for lower coordination numbers (9 for **1**–**3** and 8 for **4**–**5**). The size of Dy^{III} is appropriate to access both the structural types.

Magnetic Properties

The magnetic data for **1** are shown in Figure 6. Fitting the data for **1** required inclusion of a paramagnetic impurity term, which was fixed at a reasonable value (5% of a monomeric Co(II) impurity) by running a series of simulations in PHI.[40] The *g* value for Gd(III) was fixed to 2.0 and temperature independent paramagnetism (TIP) was fixed at 200 x 10^{-6} cm^3 mol^{-1} *per* Co(III) ion.[41] Simultaneous fitting of the χT *vs.* T data and M *vs.* H data in PHI gives: $J = -0.09$ (± 0.01) cm^{-1} (note that the obtained J value is reported according to the Hamiltonian $\hat{H} = -J(\vec{S}_1 \cdot \vec{S}_2)$ to enable easy comparison to that obtained from the theoretical studies). Both the fit to the magnetic data and the DFT studies give a weak antiferromagnetic exchange interaction between the Gd(III) centres (*vide infra*). The M *vs.* H data arise largely from field-induced population of close-lying excited spin states within the complex due to the very weak exchange interaction between Gd(III) centers.

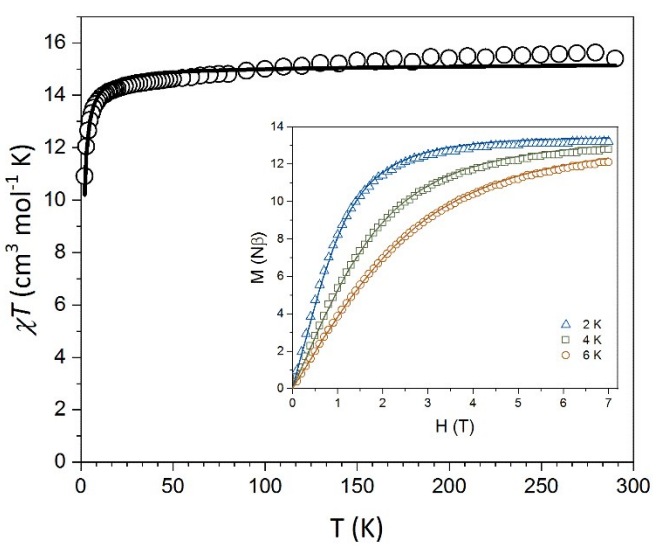

View Article Online
DOI: 10.1039/D1DT02038B

Figure 6. Temperature dependence of χT for complex **1** (black open circles). The inset shows the magnetization *vs.* field data at 2, 4 and 6 K. The solid lines correspond to a simultaneous fit of the susceptibility and magnetization data (see text for details).

The χT *vs.* T data for **2-5** are shown in Figure S24 and the fitting of that data is discussed in the section Theoretical Calculations. The M *vs.* H data and the ac susceptibility data for **2-5** are shown in Figure S17 and Figures S18 to S21. The terbium(III)-containing complex **2** and holmium(III)-containing complex **5** display no slow relaxation of the magnetization with, or without, an applied dc field. The dysprosium(III)-containing complex **3** and the dysprosium(III)/cobalt(II)-containing complex **4** display the onset of slow relaxation of the magnetization at low temperature in zero dc field; there was no maxima observed upon addition of a dc field and no further ac studies could be carried out. The observed AC susceptibility behaviour for all complexes is consistent with the theoretical studies except for **3** and **4** (*vide infra*).

Theoretical calculations

Contemporary approach to evaluate magnetic anisotropy and magnetic interactions in metal complexes is based on DFT and CASSCF calculations. First, DFT level of theory was utilized for assessing the isotropic exchange between two Gd^{III} ions in compound **1** with the help of ORCA 4.2 software. Thus, the high-spin state and the broken-symmetry states were calculated with PBE0 hybrid functional using relativistic DKH basis sets for this version of Heisenberg spin Hamiltonian, $\hat{H} = -J(\vec{S}_1 \cdot \vec{S}_2)$, and the energy difference between high-spin (HS) and broken-symmetry (BS) spin states, $\Delta = E_{BS} - E_{HS}$, was found to be $\Delta = -4.306$ cm^{-1}. Subsequently, the exchange coupling J-parameter was calculated by Yamaguchi's approach[42] as

$$J = 2\Delta/\left(\langle S^2\rangle_{HS} - \langle S^2\rangle_{BS}\right) \cdots (3)$$

and adopts value of $J = -0.18$ cm^{-1}, which suggests weak antiferromagnetic exchange and is consistent with the experimental finding. The calculated spin density of BS state is depicted in Figure 7.

View Article Online
DOI: 10.1039/D1DT02038B

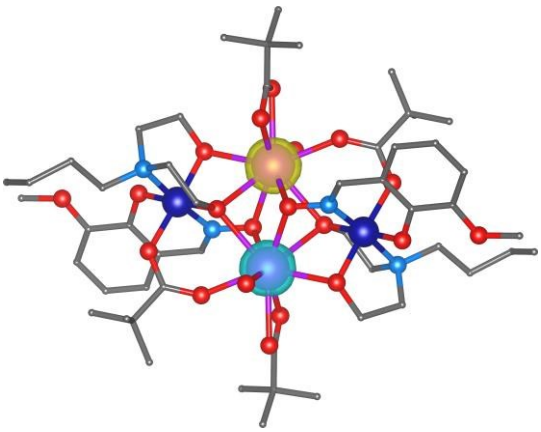

Figure 7. The calculated spin density distribution using PBE0 for **1** for the broken-symmetry state. Positive and negative spin density is represented by yellow and cyan surfaces, respectively. The isodensity surfaces are plotted with the cut-off value of 0.02 ea_0^{-3}. Hydrogen atoms are omitted for clarity.

In case of compounds **2-5**, the ground state properties of the lanthanides ions require CASSCF calculations in order to properly capture multireference character of these ions. Therefore, OpenMOLCAS package was used for CASSCF calculations, and modules SINGLE_ANISO and POLY_ANISO for evaluating the zero-field splitting and the analysis of mutual magnetic interactions, respectively. The active space of these calculations spans the respective d or f orbitals of Co^{II} or Ln^{III} ions. In case of **4** and **5**, the molecular structures were simplified as shown in Figure S23b to make such calculations feasible. The results of CASSCF are depicted in Figure 8, in which the zero-field splitting of the atomic terms induced by the ligand field is shown – $^7F_6$ for Tb^{III}, $^6H_{15/2}$ for Dy^{III} and $^5I_8$ for Ho^{III}. Also, the levels of $^4T_{1g}$ ligand field term of Co^{II} originating from O_h symmetry of the ligand field split due to lowering the symmetry of the ligand field are shown in Figure 8. The respective energy levels and *g*-tensor values calculated with SINGLE_ANISO are listed in Tables S5 to S9. The calculations for Tb^{III} ion in **2** showed two almost energetically degenerate levels, followed by two other excited states located at 80-90 cm^{-1} (Table S5). Analogous situation is found also for Ho^{III} in **5**, where pseudo doublets can be identified and are separated by circa 20 cm^{-1} (Table S5). Both Tb^{III} and Ho^{III} ions are non-Kramers ions, therefore tunneling gap (Δ_{tun}) within these pairs of states serves as indicator of the quantum tunneling of the magnetization.[43] Unfortunately, Δ_{tun} is large for both Tb^{III} and Ho^{III} ions in **2** and **5** (Table S5), which could explain lack of slow relaxation of the magnetization in AC susceptibility data. In case of Dy^{III} ions of **3** and **4**, the ground state possesses the axial type

View Article Online
DOI: 10.1039/D1DT02038B

of the magnetic anisotropy ($g_z >> g_{x,y}$), but the values of $g_{x,y}$ are larger than 0.00, which indicates significant predisposition for the quantum tunneling of the magnetization confirmed also by relatively large values of transition magnetic moment matrix elements (Tables S6 to S7). Moreover, lowest excited states are very close, 66 cm^{-1} for **3** and 19.2 cm^{-1} for **4**, which shows that local geometries of coordination polyhedra for these ions reduced the potential for large magnetization reversal barriers. This is also visualized in the plots of the magnetization blocking barrier for **3** and **4** produced by SINGLE_ANISO module (Figure S22). The axes of *g*-tensors are showed in Figure S23. Similarly, other Kramers type ions, Co^{II} in **4** and **5** have quite large $g_{x,y}$ parameters, which does not inhibit the quantum tunneling of the magnetization, thus despite the quite promising energies of the first excited states, 215 cm^{-1} in **4** and 202 cm^{-1} in **5**, it is hard to expect their positive contribution to the slow relaxation of the magnetization (Tables S8 to S9).

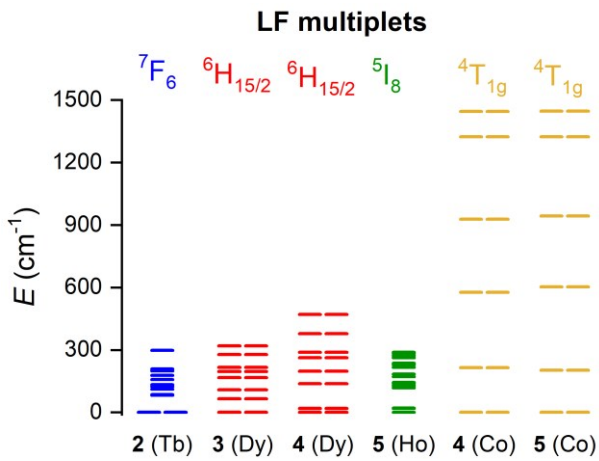

Figure 8. The output of the CASSCF calculations with CAS(8,7) for Tb^{III} in **2**, with CAS(9,7) for Dy^{III} in **3** and **4**, with CAS(10,7) for Ho^{III} in **5** and with CAS(7,5) for Co^{II} in **4** and **5**.

Next, we analyzed the experimental susceptibility data for **2-5** with the home-made routine in cooperation with POLY_ANISO module,[44] and thus we were able to estimate 4*f*-4*f* and 3*d*-4*f* magnetic interactions in this series of the compounds. The results of fitting are depicted in Figure S24 and the values of parameters are summarized in Table 2. Weak ferromagnetic exchange between lanthanide ions (J^{exch}_{Ln-Ln}) were found in tetranuclear $Ln^{III}{}_2Co^{III}{}_2$ compounds, while antiferromagnetic exchange is present in pentanuclear $Ln^{III}{}_2Co^{II}Co^{III}{}_2$ (Table 2). The Co-Ln exchange is ferromagnetic in case of Ln = Dy, but was fitted antiferromagnetic for Ln = Ho. The variation of fitted parameters of magnetic exchange can be assigned to the variation of *f*-orbitals which are involved in mutual interactions. Moreover, we present the magnetization blocking

View Article Online
DOI: 10.1039/D1DT02038B

barrier calculated for compounds **3** and **4** for which out-of-phase signal of AC susceptibility was detected. The comparison of SINGLE_ANISO and POLY_ANISO calculations for **3** is showed in Figure 9. The matrix element of the transversal magnetic moment for Dy^{III} ion of the lowest Kramers doublet is 0.097 which is close to the limit 0.1 used to determine effective tunneling of the magnetization from CASSCF calculations. Large transversal magnetic moments between ground state and the first excited state suggest that the effective energy barrier is limited to the first excited state ($U_{eff} \leq 66$ cm^{-1}). Upon inclusion of dipolar and exchange Dy-Dy interactions, the lowest energy levels form pseudo doublets confirming prevailing antiferromagnetic interaction, ($J_{tot} = J^{exch}_{Dy-Dy} + J^{dip}_{Dy-Dy}$) < 0, and diminishing but higher that threshold (10^{-5} cm^{-1}) tunneling gaps ($\Delta_{tun} = 2.5\text{x}10^{-3}$ cm^{-1}). In case of compound **4**, the SINGLE_ANISO calculations suggest significant probability for the tunneling of the magnetization (the matrix elements of the transversal magnetic moment between lowest Kramers doublets are larger than 0.1) and low-lying excited states. The incorporation of Dy-Dy and Co-Dy dipolar and exchange interactions by POLY_ANISO resulted in formation of three close lying Kramers doublets (Figure 10) and each of them having also significant probability for the quantum tunneling.

These outcomes are in contrast to the experimental observation of out-of-phase susceptibility in **3** and **4**, however, we are aware that presented CASSCF calculations are not able to fully address all relaxation mechanisms in solid state. Differences between experimental and theoretically predicted data have also been highlighted in our previous work.[6]

Table 2. The magnetic exchange (J^{exch}) and dipolar interactions (J^{dip}) derived from analysis of magnetic susceptibilities for **2-5** with POLY_ANISO module

Types of magnetic interaction (cm^{-1})	**2**	**3**	**4**		**5**	
	J_{Tb-Tb}	J_{Dy-Dy}	J_{Dy-Dy}	J_{Co-Dy}	J_{Ho-Ho}	J_{Co-Ho}
J^{dip}	–0.089	–0.177	0.000	0.000	–0.025	0.000
J^{exch}	+0.002	+0.122	–1.602	+3.180	–0.020	–0.390
J_{tot}	-0.087	–0.055	–1.602	+3.180	–0.045	–0.390

View Article Online
DOI: 10.1039/D1DT02038B

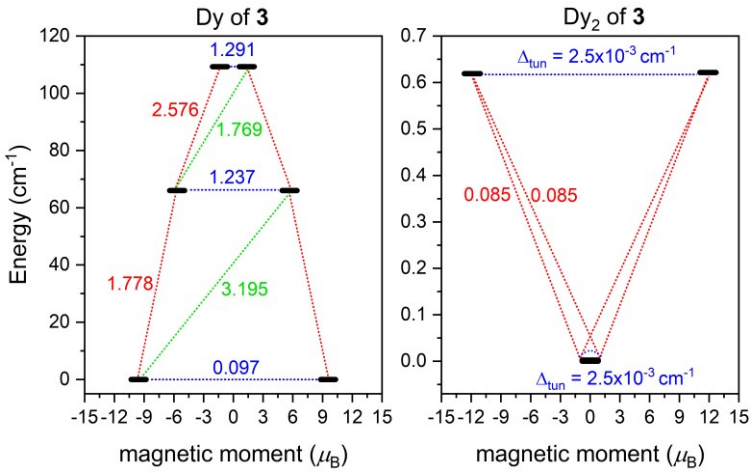

Figure 9. Magnetization blocking barrier in **3** calculated for Dy^{III} by SINGLE_ANISO (*left*) and for Dy^{III}-Dy^{III} by POLY_ANISO using J^{exch}_{Dy-Dy} = = +0.122 cm^{-1} and J^{dip}_{Dy-Dy}= –0.177 cm^{-1} (*right*). The numbers presented in plot represent the corresponding matrix element of the transversal magnetic moment, and the Δ_{tun} shows the tunneling gap of the indicated doublets.

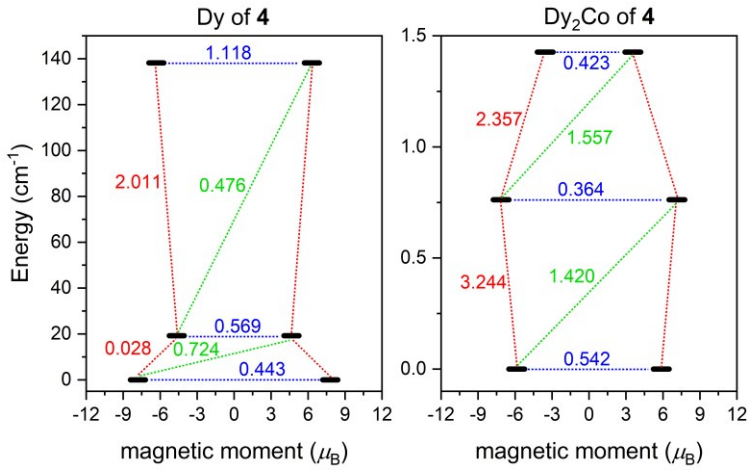

Figure 10. Magnetization blocking barrier in **4** calculated for Dy^{III} by SINGLE_ANISO (*left*) and for Dy^{III}-Dy^{III}-Co^{II} by POLY_ANISO using exchange (J^{exch}) and dipolar (J^{dip}) interactions listed in Table 2 (*right*). The numbers presented in plot represent the corresponding matrix element of the transversal magnetic moment.

Conclusions

The synthesis and isolation of five new cobalt-lanthanide coordination aggregates from the use of two different ligands H_2L and N–BuDEAH_2 together, has increased our understanding about the synthetic methods and the reaction sequences required to obtain such compounds. A shift in preference from *tetranuclear* to *pentanuclear* structure across the lanthanide series, projected,

View Article Online
DOI: 10.1039/D1DT02038B

the influence the size of the Ln^{III} ions can have on the nuclearity of coordination clusters and the consequent importance of the lanthanide contraction on the synthesis of polynuclear molecules. Furthermore the change in sequence of ligand addition opened up the pathway for accessing both structural types in the case of Dy^{III}. HRMS (+ve) analysis of solutions revealed the differential cleavage of $Co_2(\mu\text{-}OH_2)(O_2CCMe_3)_4(HO_2CCMe_3)_4$ by the two ligands and helped understand the aggregation process under different sequence of reactant addition. The *tetranuclear* $Ln^{III}{}_2Co^{III}{}_2$ complexes exhibit a butterfly like topology with a more complex bridging network having the metal ion centers lying in a plane. On the other hand in the *pentanuclear* $Ln^{III}{}_2Co^{II}Co^{III}{}_2$ complexes, an additional Co^{II} ion is trapped in the structure destroying the planar arrangement of the metal ions. Due to the presence of large number of solvent molecules within the crystal lattice of the $Ln^{III}{}_2Co^{III}{}_2$ aggregates, an extensive hydrogen bonding network was observed. Fitting of the magnetic data for **1** gives a weak antiferromagnetic exchange interaction between the Gd^{III} ions, which is confirmed by the theoretical calculations carried out with a PBE0 hybrid functional. The rest of the reported compounds were treated at CASSCF level of theory. Subsequent analysis of experimental magnetic data with POLY_ANISO module revealed variation of the dipole-dipole and the exchange interactions of the types Ln-Ln and Ln-Co within the series suggesting fast relaxation of the magnetization. But this is in contrast to the out-of-phase signals observed in AC susceptibility measurements observed for **3** and **4**. Theoretical predictions are in line with the experimentally observed lack of slow relaxation in **2** and **5**.

Electronic Supporting Information

X-ray crystallographic data in CIF format, Tables S1–S9, Figures S1–S24, Chart S1, Schemes S1−S2. CCDC–2090138, 2090137, 2090139, 2090141, 2090140 contain the supplementary crystallographic data in CIF format for complexes **1**–**5**.

Conflict of interests

The authors declare no competing financial interests.

Acknowledgements

D. B. would like to thank IIT Kharagpur for research facility and his fellowship. R. H. acknowledges the financial support from the institutional sources of the Department of Inorganic Chemistry, Palacký University Olomouc, Czech Republic and supply of computational resources

View Article Online
DOI: 10.1039/D1DT02038B

by the project "e-Infrastruktura CZ" (e-INFRA LM2018140) provided within the program Projects of Large Research, Development and Innovations Infrastructures. M. M. thanks the University of Glasgow for financial support.

References

1. (a) R. E. P. Winpenny *J. Chem. Soc., Dalton Trans.*, 2002, 1–10. (b) M. Manoli, S. Alexandrou, L. Pham, G. Lorusso, W. Wernsdorfer, M. Evangelisti, G. Christou and A. J. Tasiopoulos, *Angew. Chem., Int. Ed.*, 2016, **55**, 679–684. (c) J. M. Frost, F. J. Kettles, C. Wilson and M. Murrie, *Dalton Trans.*, 2016, **45**, 18094–18097. (d) D. Maniaki, E. Pilichos and S. P. Perlepes, *Front. Chem.*, 2018, **6**, 461–488.

2. H.-L. Zheng, X.-L. Chen, T. Li, Z. Yin, Y. Zhang, M. Kurmoo, M.-H. Zeng, *Chem. Eur. J.*, 2018, **24**, 7906–7912.

3. H. X. Na, P. Y. Yang, Z. Yin, Y. H. Wang, L. X. Chang, R. Si, M. Kurmoo, M. H. Zeng, *Chem. Eur. J.* 2016, **22**, 18404–18411.

4. Y.-Q. Hu, M.-H. Zeng, K. Zhang, S. Hu, F.-F. Zhou, M. Kurmoo, *J. Am. Chem. Soc.*, 2013, **135**, 7901–7908.

5. (a) D. Basak, J. v. Leusen, T. Gupta, P. Kögerler, D. Ray, *Dalton Trans.*, 2020, **49**, 7576–7591. (b) D. Basak, E. R. Martí, M. Murrie, I. Nemec and D. Ray, *Dalton Trans.*, 2021, **50**, 9574–9588.

6. D. Basak, J. v. Leusen, T. Gupta, P. Kögerler, V. Bertolasi, D. Ray, *Inorg. Chem.*, 2020, **59**, 2387–2405 and references therein.

7. H. N. Miras, E. F. Wilson, L. Cronin, *Chem. Commun.*, 2009, 1297–1311.

8. (a) X. L. Chen, H. B. Xu, X. X. Shi, Y. Zhang, T. Yang, M. Kurmoo, M. H. Zeng, *Inorg. Chem.*, 2017, **56**, 14069–14076. (b) G. J. T. Cooper , G. N. Newton , P. Kögerler , D.-L. Long , L. Engelhardt , M. Luban and L. Cronin , *Angew. Chem., Int. Ed.*, 2007, **46**, 1340–1344. (c) G. N. Newton , G. J. T. Cooper , P. Kögerler , D.-L. Long and L. Cronin , *J. Am. Chem. Soc.*, 2008, **130** , 790–791.

9. (a) R.-F. Jin, S.-Y. Yang, H.-M. Li, L.-S. Long, R.-B. Huang and L.-S. Zheng, *CrystEngComm*, 2012, **14**, 1301–1316. (b) P. Chen, H. Chen, P. Yan, Y. Wang and G. Li, *CrystEngComm*, 2011, **13**, 6237–6242. (c) M. N. Akhtar, Y.-Z. Zheng, Y. Lan, V. Mereacre, C. E. Anson and A. K. Powell, *Inorg. Chem.*, 2009, **48**, 3502–3504. (d) M. N. Akhtar, Y.

View Article Online
DOI: 10.1039/D1DT02038B

H. Lan, V. Mereacre, R. Clerac, C. E. Anson and A. K. Powell, *Polyhedron*, 2009, **28**, 1698–1703.

10. (a) R. Sessoli and A. K. Powell, *Coord. Chem. Rev.*, 2009, **253**, 2328–2341. (b) D. N. Woodruff, R. E. P. Winpenny and R. A. Layfield, *Chem. Rev.*, 2013, **113**, 5110–5148.

11. (a) J. Rinck, G. Novitchi, W. Van den Heuvel, L. Ungur, Y. Lan, W. Wernsdorfer, C. E. Anson, L. F. Chibotaru and A. K. Powell, *Angew. Chem., Int. Ed.*, 2010, **49**, 7583–7587. (b) A. McRobbie, A. R. Sarwar, S. Yeninas, H. Nowell, M. L. Baker, D. Allan, M. Luban, C. A. Muryn, R. G. Pritchard, R. Prozorov, G. A. Timco, F. Tuna, G. F. S. Whitehead and R. E. P. Winpenny, *Chem. Commun.*, 2011, **47**, 6251–6253.

12. S. K. Langley, N. F. Chilton, B. Moubaraki and K. S. Murray, *Inorg. Chem.*, 2013, **52**, 7183–7192.

13. L. Rigamonti, N. Bridonneau, G. Poneti, L. Tesi, L. Sorace, D. Pinkowicz, J. Jover, E. Ruiz, R. Sessoli, A. Cornia, *Chem. Eur. J.*, 2018, **24**, 8857–8868.

14. Kuduva R. Vignesh, Stuart K. Langley, Keith S. Murray, and Gopalan Rajaraman, *Inorg. Chem.*, 2017, **56**, 2518–2532.

15. (a) Q. F. Sun, S. Sato, M. Fujita, *Angew. Chem. Int. Ed.*, 2014, **53**, 13510–13513. (b) N. K. Al-Rasbi, I. S. Tidmarsh, S. P. Argent, H. Adams, L. P. Harding, M. D. Ward, *J. Am. Chem. Soc.*, 2008, **130**, 11641–11649.

16. (a) Y. Li, Y. Qin, Y. Wang, W. Liu, Y. Li, *Polyhedron*, 2016, **111**, 156–160. (b) F.-S. Guo , J.-L. Liu, J.-D. Leng, Z.-S. Meng , Z.-J. Lin, M.-L. Tong, S. Gao, L. Ungur, L. F. Chibotaru, *Chem. Eur. J.*, 2011, **17**, 2458–2466. (c) I. A. Kühne, N. Magnani, V. Mereacre, W. Wernsdorfer, C. E. Anson, A. K. Powell, *Chem. Commun.*, 2014, **50**, 1882–1885. (d) I. A. Kühne, V. Mereacre, C. E. Anson, Annie K. Powell, *Chem. Commun.*, 2016, **52**, 1021–1024. (e) M. Hołyńska, D. Premužić, I.-R. Jeon, W. Wernsdorfer, R. Clérac, S. Dehnen, *Chem. Eur. J.*, 2011, **17**, 9605–9610. (f) I. J. Hewitt, Y. Lan, C. E. Anson, J. Luzon, R. Sessoli and A. K. Powell, *Chem. Commun.*, 2009, 6765–6767.

17. (a) V. Mereacre, M. N. Akhtar, Y. Lan, A. M. Ako, R. Clérac, C. E. Anson, A. K. Powell, *Dalton Trans.*, 2010, **39**, 4918–4927. (b) A. M. Ako, V. Mereacre, R. Clérac, I. J. Hewitt, Y. Lan, G. Buth, C. E. Anson, A. K. Powell, *Inorg. Chem.* 2009, **48**, 6713–6723. (c) A. M. Ako, V. Mereacre, R. Clérac, I. J. Hewitt, Y. Lan, C. E. Anson, A. K. Powell, *Dalton Trans.*, 2007, 5245–5247.

View Article Online
DOI: 10.1039/D1DT02038B

18. (a) L. Sorace, C. Benelli, D. Gatteschi, *Chem. Soc. Rev.*, 2011, **40**, 3092–3104. (b) A. K. Bar, C. Pichon, J.-P. Sutter, *Coord. Chem. Rev.*, 2016, **308**, 346–380. (c) F. Habib, M. Murugesu, *Chem. Soc. Rev.*, 2013, **42**, 3278–3288. (d) P. Zhang, Y.-N. Guo, J. Tang, *Coord. Chem. Rev.*, 2013, **257**, 1728–1763. (e) S. G.-Coca, D. Aravena, R. Morales, E. Ruiz, *Coord. Chem. Rev.*, 2015, **289-290**, 379–392. (f) S. K. Langley, L. Ungur, N. F. Chilton, B. Moubaraki, L. F. Chibotaru, K. S. Murray, *Inorg. Chem.*, 2014, **53**, 4303–4315. (g) A. V. Funes, L. Carrella, E. Rentschler, P. Albores, *Dalton Trans.*, 2014, **43**, 2361–2364. (h) A. V. Funes, L. Carrella, Y. Rechkemmer, J. v. Slageren, E. Rentschler, P. Albores, *Dalton Trans.*, 2017, **46**, 3400–3409. (i) S. K. Langley, C. Le, L. Ungur, B. Moubaraki, B. F. Abrahams, L. F. Chibotaru, K. S. Murray, *Inorg. Chem.*, 2015, **54**, 3631–3642. (j) S. K. Langley, N. F. Chilton, B. Moubaraki, K. S. Murray, *Inorg. Chem. Front.*, 2015, **2**, 867–875. (k) S. K. Langley, N. F. Chilton, B. Moubaraki, K. S. Murray, *Inorg. Chem.*, 2013, **52**, 7183–7192.

19. H. Chen, C.-B. Ma, M.-Q. Hu, H.-M. Wen, C.-N. Chen, *Dalton Trans.*, 2014, **43**, 16737–16744.

20. G. Aromi, A. S. Batsanov, P. Christian, M. Helliwell, A. Parkin, S. Parsons, A. A. Smith, G. A. Timco and R. E. P. Winpenny, *Chem. Eur. J.*, 2003, **9**, 5142.

21. (a) F. Neese, *Comput. Mol. Sci.*, 2012, **2**, 73–78. (b) F. Neese, *Comput. Mol. Sci.*, 2018, **8**, e1327. (c) F. Neese, F. Wennmohs, U. Becker and C. Riplinger, J. Chem. Phys., 2020, **152**, 224108.

22. C. Adamo and V. Barone, *J. Chem. Phys.*, 1999, **110**, 6158.

23. (a) F. Weigend and R. Ahlrichs, *Phys. Chem. Chem. Phys.*, 2005, **7**, 3297–3305. (b) D. Aravena, F. Neese and A. P. Dimitrios. *J. Chem. Theory Comput.*, 2016, **12**, 1148–1156.

24. (a) M. Douglas and N. M. Kroll, *Ann. Phys. (N. Y).* 1974, **82**, 89–155. (b) B. A. Hess, *Phys. Rev. A*, 1986, **33**, 3742–3748.

25. L. Visscher and K. G. Dyall, *Atom. Data Nucl. Data Tables*., 1997, **67**, 207–224.

26. D. A. Pantazis and F. Neese, *J. Chem. Theory Comput.*, 2009, **5**, 2229–2238.

27. (a) F. Neese, F. Wennmohs, A. Hansen and U. Becker, *Chem. Phys.*, 2009, **356**, 98–109. (b) R. Izsák and F. Neese, *J. Chem. Phys.*, 2011, **135**, 144105.

28. C. F. Macrae, I. Sovago, S. J. Cottrell, P. T. A. Galek, P. McCabe, E. Pidcock, M. Platings, G. P. Shields, J. S. Stevens, M. Towler and P. A. Wood, *J. Appl. Cryst.*, 2020, **53**, 226–235.

29. K. Momma and F. Izumi, *J. Appl. Crystallogr*., 2011, **44**, 1272–1276.

View Article Online
DOI: 10.1039/D1DT02038B

30. I. F. Galván, M. Vacher, A. Alavi, C. Angeli, F. Aquilante, J. Autschbach, J. J. Bao, S. I. Bokarev, N. A. Bogdanov, R. K. Carlson, L. F. Chibotaru, J. Creutzberg, N. Dattani, M. G. Delcey, S. S. Dong, A. Dreuw, L. Freitag, L. M. Frutos, L. Gagliardi, F. Gendron, A. Giussani, L. González, G. Grell, M. Guo, C. E. Hoyer, M. Johansson, S. Keller, S. Knecht, G. Kovačević, E. Källman, G. L. Manni, M. Lundberg, Y. Ma, S. Mai, J. P. Malhado, P. Å. Malmqvist, P. Marquetand, S. A. Mewes, J. Norell, M. Olivucci, M. Oppel, Q. M. Phung, K. Pierloot, F. Plasser, M. Reiher, A. M. Sand, I. Schapiro, P. Sharma, C. J. Stein, L. K. Sørensen, D. G. Truhlar, M. Ugandi, L. Ungur, A. Valentini, S. Vancoillie, V. Veryazov, O. Weser, T. A. Wesołowski, P.–O. Widmark, S. Wouters, A. Zech, J. P. Zobel and R. Lindh, *J. Chem. Theory Comput.*, 2019, **15**, 5925–5964.

31. B. O. Roos, R. Lindh, P.–Å. Malmqvist, V. Veryazov, P.–O. Widmark and A. C. Borin, *J. Phys. Chem. A*, 2008, **112**, 11431–11435.

32. *Saint, Smart and XPREP*, Siemens Analytical X-ray Instruments Inc., Madison, WI, 1995

33. G. M. Sheldrick, *SHELXS-2014*, University of Göttingen, Göttingen, Germany, 2014.

34. G. M. Sheldrick, *Acta Crystallogr.,Sect. A: Found. Crystallogr*., 2008, **64**, 112−122.

35. L. J. Farrugia, *J. Appl. Crystallogr*., 2012, **45**, 849−854.

36. G. M. Sheldrick, *SADABS Software for Empirical Absorption Correction*, University of Göttingen, Institute fur Anorganische Chemieder Universitat, Göttingen, Germany, 1999−2003.

37. A. Formanuik, A.-M. Ariciu, F. Ortu, R. Beekmeyer, A. Kerridge, F. Tuna, E. J. L. McInnes and David P. Mills, *Nat. Chem.*, 2017, **9**, 578–583

38. *DIAMOND, Visual Crystal Structure Information System, version 3.1*, Crystal Impact, Bonn, Germany, 2004.

39. (a) I. D. Brown and D. Altermatt, *Acta Crystallogr., Sect. B: Struct. Sci.*, 1985, **41**, 244−247. (b) I. D. Brown, *Chem. Rev.*, 2009, **109**, 6858−6919.

40. N. F. Chilton, R. P. Anderson, L. D. Turner, A. Soncini and K. S. Murray, *J. Comput. Chem.*, 2013, **34**, 1164–1175.

41. R. L. Carlin, in *Magnetochemistry*, Springer–Verlag, Berlin Heidelberg, 1986.

42. (a) K. Yamaguchi, Y. Takahara and T. Fueno, in *Applied Quantum Chemistry*, ed. V. H. Smith, Reidel, Dordrecht, 1986, pp. 155. (b) T. Soda, Y. Kitagawa, T. Onishi, Y. Takano, Y. Shigeta, H. Nagao, Y. Yoshioka and K. Yamaguchi, *Chem. Phys. Lett.*, 2000, **319**, 223–230.

View Article Online
DOI: 10.1039/D1DT02038B

43. J. Wang, J. J. Zakrzewski, M. Zychowicz, V. Vieru, L. F. Chibotaru, K. Nakabayashi, S. Chorazy and S.-i. Ohkoshi, *Chem. Sci.*, 2021, **12**, 730–741.

44. (a) L. F. Chibotaru, L. Ungur and A. Soncini, *Angew. Chemie Int. Ed.*, 2008, **47**, 4126–4129. (b) L. F. Chibotaru and L. Ungur, *J. Chem. Phys.*, 2012, **137**, 064112. (c) L. Ungur, M. Thewissen, J.–P. Costes, W. Wernsdorfer and L. F. Chibotaru, *Inorg. Chem.*, 2013, **52**, 6328–6337.